Acta Astronautica 214 (2024) 30–45

Contents lists available at ScienceDirect

Acta Astronautica

journal homepage: www.elsevier.com/locate/actaastro

Research paper

Effects of model fidelity and uncertainty on a model-based attitude controller for satellites with flexible appendages

Robert Gordon *, Matteo Ceriotti, Kevin Worrall

James Watt School of Engineering, University of Glasgow, Glasgow, G12 8QQ, United Kingdom

ARTICLE INFO

Keywords:
Inverse simulation
Attitude control
Flexible appendages

ABSTRACT

This paper investigates the effects of model fidelity and parameter uncertainty on the performance of a hybrid model-based feedback-feedforward control scheme for attitude tracking of a satellite with flexible appendages. The feedforward component is an inverse model-based term produced through a computational approach known as inverse simulation (InvSim), which works by iteratively solving a discretised reference trajectory. The hybrid controller's feedback is proportional-derivative (PD) based, using body attitude and rate feedback to provide stability and robustness. Furthermore, to ensure that the flexible modes do not trigger instability, the PD control gains are tuned to give a closed-loop response that is significantly slower than the flexible modes. Additionally, excitation of the flexible modes is reduced by minimising jerk through polynomial rest-to-rest manoeuvres, following the shortest quaternion path using spherical–linear-interpolation (SLERP). The effects of the appendage flexing on attitude tracking are then compensated through the feedforward element of the hybrid controller, with performance being compared to a traditional PD tracking law. The effect of the model fidelity on the performance of the hybrid controller is investigated through the use of both rigid body and multiple-fidelity finite-element mathematical models. Additionally, the effect of uncertainties in the model parameters is investigated to determine the accuracy of the model required to obtain significant improvement in attitude tracking. It is found that in the absence of any model parameter uncertainty, the hybrid controller outperforms the PD tracking control law by at least one order of magnitude when the finite-element model is used. Increasing the number of finite elements was found to provide no significant improvement in performance, with one element being sufficient and favourable with its lower computational overhead. It was also found that to ensure good performance compared to the PD tracking controller, the uncertainty in the inertia tensor should be <1%. Similarly, uncertainty in the first flexible modal frequency should be <0.5 rad/s.

1. Introduction

A common approach to increasing satellites' capabilities, whilst minimising mass and size for economical launch cost, is to utilise deployable structures and appendages attached to a central main hub. These structures and appendages commonly introduce flexible dynamic modes to the attitude dynamics and thus must be considered and compensated for to ensure good pointing accuracy during attitude manoeuvres.

One simple method to minimise the effects of the flexible modes is to try and avoid them as much as possible. This can be achieved by carefully selecting the attitude and body rate references to ensure that the manoeuvres' jerk (the derivative of acceleration) is minimised. For example, a time-optimal bang–bang manoeuvre, which contains infinite jerks at each instantaneous change in acceleration, can be modified through the use of *versine* functions [1,2]. This is shown to reduce the excitation of the flexible modes and the disturbance torques they induce on the main satellite body. Alternatively, a polynomial-based reference can also be used to produce a low jerk profile [3], at the expense of increasing the time or maximum acceleration of the manoeuvre. Additionally, a model-based method known as input-shaping can further suppress the flexible modes of the satellite's appendages [1,4,5]. This works through the convolution of the control input with a set of impulses that cancel the flexible modes through the addition of zeros at the exact locations of the poles of the flexible modes [5].

For the case of attitude tracking, strict adherence to pointing constraints and robustness may be of greater concern. Sliding mode control (SMC) is a nonlinear control method commonly used for attitude-tracking problems and has been applied to satellites with flexible appendages [6–8]. The basic principle is to define a sliding surface or

* Corresponding author.
E-mail address: r.gordon.5@research.gla.ac.uk (R. Gordon).

https://doi.org/10.1016/j.actaastro.2023.10.011
Received 2 June 2023; Received in revised form 4 August 2023; Accepted 11 October 2023
Available online 14 October 2023

hyperplane, upon which the system will be forced towards an equilibrium. Then a discontinuous term drives the system onto the surface and ensures that disturbances are accounted for. One approach [6] uses the internal reaction torque at the root of the appendage as part of the sliding surface. This ensures the stability of the flexible modes, however, assumes that the internal torque can be measured through some sort of strain gauge or estimated. Another method [7] is to simply augment the SMC with active vibration suppression through the use of piezoelectric smart materials, which are placed along the length of the appendage and controlled with a second controller. This deals with the flexible modes that may be excited due to chattering, characteristic of SMC. A more recent paper [8] deals with the chattering problem by replacing the usual discontinuous switching term with an adaptive control element. This ensures a more smooth control action when passing through the sliding surface, avoiding excitation of the appendages. This paper also requires torques to be applied both to the appendages and the main body, rather than being applied to the main body only.

Model-based methods, such as model-predictive-control (MPC) [9–11], have also successfully been applied to attitude control of satellites with flexible appendages. MPC iteratively solves a constrained optimisation problem in real-time to converge upon a control law. The constraints are usually given by a simplified model and a cost function, consisting of a combination of control and state terms, is minimised such that a given performance criteria is satisfied. MPC has been applied for single-axis attitude slew manoeuvres, making use of single-input-multiple-output (SIMO) reduced models [9,10]. One approach [9] additionally makes use of a genetic algorithm to tune the MPC control parameters to obtain a desirable response in terms of rise time, settling time, overshoot and flexible mode amplitudes. Another approach [11] re-linearises a nonlinear model at each control step, which can then be used by the MPC to perform 3-axis earth pointing and spin-up manoeuvres. It was found that the MPC [11] was highly sensitive to uncertainty in the model parameters, an aspect that will also be investigated in this work. Additionally, a common limitation of all of the MPC approaches above is an assumption that the full state vector can be measured or estimated, including the flexible modes.

An alternative, but common, approach for improved tracking performance is to employ a feedforward control element which can be added to an existing feedback controller [12,13], and allow compensation for modelled disturbances [14]. Therefore with a model that sufficiently describes the flexible dynamics of the appendages, it is suggested that their effects on attitude tracking can be compensated for. To produce this feedforward term, a suitable model inversion technique can be used. The most popular is Nonlinear Dynamic Inversion (NDI), also commonly used for feedback-linearisation [15,16]. This technique requires analytical differentiation of the system's dynamic equations to achieve a mapping of desired output states to the required inputs/controls. For a complex model, this can be highly laborious and requires a re-derivation if any significant changes are made to the model, or if the model is being changed entirely. An alternative computational approach known as Inverse Simulation (InvSim) can also be used [17]. The most common method of InvSim, the integral method [18,19], is based upon the discretisation of the reference trajectory which is then iteratively solved using a numerical method, commonly the Newton–Raphson method. This usually requires the calculation of a Jacobian or Hessian through numerical differencing, which leads to high computational overheads. It has been shown that InvSim performs as well as, or in some cases better than NDI [20]. However, the main benefit of InvSim is that its numerical process treats the system model as a black box. It can therefore easily be used with any existing model that may be available and does not need to be modified if changes are made to the model. InvSim should therefore be capable of producing a feedforward element with any existing model that can improve attitude tracking of an existing feedback controller, which while expensive in terms of computational time, is cheap in terms of development time.

The integral InvSim method can also be used as a preliminary controller during the iterative design process or during feasibility studies. Using the InvSim algorithm, limitations of the system's dynamics can be established and the sizing of the actuators can be validated. Once the final system has been designed, a traditional control approach could be used, now only having to be developed and configured once, or the InvSim solution could still be used as a feedforward element to improve attitude tracking as is shown in this work.

Application of InvSim as a feedforward controller has previously been explored [21]. It has been shown to be capable of producing an effective feedforward term, improving tracking performance when applied to both a linearised multi-input-multi-output (MIMO) helicopter model, and a nonlinear single-input-single-output (SISO) model of a boat. The work uses this InvSim feedforward controller with an H^{∞} feedback controller, which ensures robustness to measurement noise and output disturbances. This work will look to employ a similar *hybrid* control strategy with a proportional-derivative (PD) feedback controller instead of H^{∞}. PD is used as this is highly common within the attitude control literature [22,23].

This paper will show that the addition of a model-based feedforward, to a traditional PD attitude controller, can be achieved easily through the use of InvSim, improving attitude tracking through consideration of the flexible appendage dynamics, and avoiding the greater effort of other model inversion techniques such as NDI. In this work, particular interest is also paid to the fidelity of the model being used to produce the InvSim feedforward control element. Previous work has investigated the effects of parameter uncertainty [24] on the effectiveness of InvSim-based control, however no quantitative investigation into the effects of the fidelity of the model being used by InvSim has been explored. It is usually assumed that the model being computationally inverted by InvSim is of sufficient fidelity to provide an accurate control solution for the user's purposes, which may not be true in the case of high model uncertainty [25]. Increasing the fidelity of a model representing a satellite with flexible appendages will tend to introduce higher frequency dynamics, requiring the use of a smaller integration step size to ensure the numerical stability of the InvSim. This can result in an increase in the computational overhead, and therefore a study as to the effects of model fidelity on the performance of the hybrid control scheme should be first quantified. This allows for an informed decision to be made as to the fidelity of the model that should be used, given accuracy requirements and computational availability.

Mathematical modelling of satellites with flexible appendages can be achieved through several approaches, including considering the satellite a rigid body, assemblage of rigid bodies, or as a combination of rigid and elastic bodies [26]. Most commonly, the satellite is considered a rigid body with flexible appendages attached that can be idealised as plates [27] or beams [6]. The vibration dynamics of these beams and plates are governed by partial differential equations, which must first be discretised through an appropriate method. This will result in a set of ordinary differential equations which can then be easily solved through numerical integration. One such discretisation approach treats a beam as a series of lumped-mass elements connected by torsional spring dampers to reproduce the flexible dynamics [2,28]. Another method of discretisation, commonly used in engineering, is the finite-element approach [29,30]. As the number of elements, N_e, used to represent each beam is increased, the number of flexible modes in the model will increase and will become more accurate. A simple finite-element model will be used in this work to allow for the fidelity of the model to be modified simply by varying the number of elements used to represent each appendage. Additionally, a continuous model that uses an analytical solution for the modal shapes and frequencies [31] will be used as the "real" system for testing.

The paper is organised as follows. First, models of varying fidelity will be developed to allow for the model fidelity analysis to be completed. The InvSim algorithm used will briefly be described before

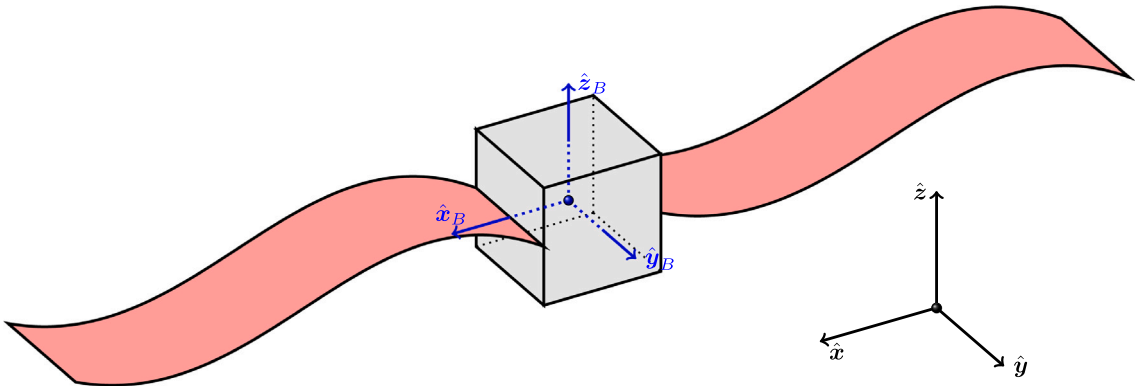

Fig. 1. Satellite with two flexible appendages.

a low-jerk path planning method is proposed to minimise excitation of the flexible dynamic modes. Next, both the baseline PD tracking controller is presented, with the closed loop dynamics analysed to allow for appropriate gain tuning. The hybrid controller with InvSim feedforward and linear PD feedback is then presented. The performance of the model-based hybrid controller will then be compared to the PD tracking law through the use of Monte-Carlo simulations and sensitivity analysis, assessing the effects of model fidelity and uncertainty on the attitude tracking performance.

2. Multi-fidelity mathematical modelling

The mathematical models used in this work are of varying fidelity and can be used to assess the effects on the performance of the model-based controller. The specific satellite configuration can be seen in Fig. 1, and consists of two symmetric flexible appendages and four reaction wheel actuators. The first model considers the satellite as one rigid body, ignoring the influence of the flexible modes of the appendages. A rigid model of a satellite with reaction wheels can be expressed simply:

$$\mathbf{I}\dot{\boldsymbol{\omega}} + \mathbf{A}_w\boldsymbol{u} + [\boldsymbol{\omega}]_\times\left(\mathbf{I}\boldsymbol{\omega} + \mathbf{I}_w\boldsymbol{\omega}_w\right) = 0 \tag{1}$$

where $\mathbf{I}$ is the total inertia matrix of the satellite including the reaction wheels and appendages, $\mathbf{I}_w$ is the inertia of the reaction wheels, $\boldsymbol{\omega}_w$ is the angular rate of the reaction wheels, $\boldsymbol{\omega}$ is the body rate of the satellite, $[\cdot]_\times$ is the skew-symmetric cross-product matrix, and $\boldsymbol{u}$ is the input the system which in this case is the reaction wheel torque:

$$\mathbf{I}_w\dot{\boldsymbol{\omega}}_w = \mathbf{A}_w\boldsymbol{u} \tag{2}$$

where $\mathbf{A}_w$ is the reaction wheel distribution matrix mapping the motor inputs to the body axes. Each column of $\mathbf{A}_w$ is the unit vector direction of one reaction wheel in the set, i.e. for four wheels $\mathbf{A}_w = [\hat{\boldsymbol{w}}_1\ \hat{\boldsymbol{w}}_2\ \hat{\boldsymbol{w}}_3\ \hat{\boldsymbol{w}}_4]$, therefore the inertia of the whole reaction wheel set assuming it is centred in the rigid body:

$$\mathbf{I}_w = \sum_{j=1}^{4}\mathrm{diag}(I_w\hat{\boldsymbol{w}}_j) \tag{3}$$

where I_w is the inertia of each reaction wheel about its rotational axis, and diag$(\cdot)$ is a diagonal matrix. Additionally, the attitude representation is given through the quaternion kinematics:

$$\dot{\boldsymbol{q}}_{1:3} = \frac{1}{2}q_0\boldsymbol{\omega} + \frac{1}{2}\left[\boldsymbol{q}_{1:3}\right]_\times\boldsymbol{\omega} \tag{4a}$$

$$\dot{q}_0 = -\frac{1}{2}\boldsymbol{q}_{1:3}^T\boldsymbol{\omega} \tag{4b}$$

where $\boldsymbol{q}_{1:3}$ is the 3-element vector component and q_0 is the scalar component of the scalar first unit attitude quaternion:

$$\boldsymbol{q} = \begin{bmatrix} q_0 \\ \boldsymbol{q}_{1:3} \end{bmatrix} \tag{5}$$

Next, the flexibility of the appendages will be taken into account by considering them at first to be continuous Euler–Bernoulli beams. The total kinetic energy of the satellite, $\mathcal{T}$, can therefore be considered from first principles:

$$\mathcal{T} = \frac{1}{2}\boldsymbol{\omega}^T(t)\left(\mathbf{I}_{hub} + \mathbf{I}_w\right)\boldsymbol{\omega}(t) + \frac{1}{2}\boldsymbol{\omega}_w^T(t)\mathbf{I}_w\boldsymbol{\omega}_w(t) + \boldsymbol{\omega}_w^T(t)\mathbf{I}_w\boldsymbol{\omega}(t) + \\ + \frac{1}{2}\rho_1\int_0^{L_1}\dot{\boldsymbol{r}}_1^T(x,t)\dot{\boldsymbol{r}}_1(x,t)\,dx + \frac{1}{2}\rho_2\int_0^{L_2}\dot{\boldsymbol{r}}_2^T(x,t)\dot{\boldsymbol{r}}_1(x,t)\,dx \tag{6}$$

where $\boldsymbol{\omega}$ is the body rate of the satellite, $\boldsymbol{\omega}_w$ is the angular rate of the reaction wheels, ρ_1 and ρ_2 are the mass per unit length densities of each appendage, $\dot{\boldsymbol{r}}_1$ and $\dot{\boldsymbol{r}}_2$ are the velocities of each appendage, x is the distance along each appendage, L_1 and L_2 are the total lengths of each appendage, $\mathbf{I}_{hub}$ and $\mathbf{I}_w$ is the inertias of the rigid hub and reaction wheels respectively.

The position of the infinitesimal mass dx at each point along the ath appendage can be seen in Fig. 2 and is given as:

$$\boldsymbol{r}_a(x,t) = (d_a + x)\hat{\boldsymbol{x}}_a^B + w_a(x,t)\hat{\boldsymbol{z}}_a^B \tag{7}$$

where $\hat{\boldsymbol{x}}_a^B$ is the longitudinal direction of the appendage, and $\hat{\boldsymbol{z}}_a^B$ is the transverse direction of the appendage. The velocities can be found with consideration of the rotating body frame:

$$\dot{\boldsymbol{r}}_a(x,t) = \dot{w}_a(x,t)\hat{\boldsymbol{z}}_a^B + [\boldsymbol{\omega}]_\times\left((d_a + x)\hat{\boldsymbol{x}}_a^B + w_a(x,t)\hat{\boldsymbol{z}}_a^B\right) \tag{8}$$

where $w_a(x,t)$ is the deflection of the appendage, $\dot{w}_a(x,t)$ is the deflection rate, and d_a is the distance of the cantilever connection of the appendage from the centre of the rigid body. The deflection along the appendage can be decomposed as a summation of modes:

$$w_a(x,t) = \boldsymbol{\phi}_a^T(x)\boldsymbol{\eta}_a(t) \tag{9}$$

$$\dot{w}_a(x,t) = \boldsymbol{\phi}_a^T(x)\dot{\boldsymbol{\eta}}_a(t) \tag{10}$$

where $\boldsymbol{\eta}_a$ and $\dot{\boldsymbol{\eta}}_a$ are nondimensional displacement and velocities of the flexible modes, and $\boldsymbol{\phi}_a(x)$ are the shape functions:

$$\boldsymbol{\phi}_a(x) = \begin{bmatrix}\phi_{a,1}(x) & \phi_{a,2}(x) & \cdots & \phi_{a,m}(x) & \cdots & \phi_{a,N_\phi}(x)\end{bmatrix}^T \tag{11}$$

where $\phi_{a,m}(x)$ is the mth mode of the ath appendage, N_ϕ is the number of modes included in this model. This simplifies the derivation of the dynamics as only $\dot{\boldsymbol{\eta}}_a$ is time dependent.

Similarly the potential energy in each appendage can be given as:

$$\mathcal{V} = \frac{1}{2}\boldsymbol{\eta}_1^T(t)\mathbf{K}_1\boldsymbol{\eta}_1(t) + \frac{1}{2}\boldsymbol{\eta}_2^T(t)\mathbf{K}_2\boldsymbol{\eta}_2(t) \tag{12}$$

where the stiffness of the continuous appendage is given as:

$$\mathbf{K}_a = EI_a\int_0^{L_a}\left(\frac{\partial^2\boldsymbol{\phi}_a(x)}{\partial x^2}\right)\left(\frac{\partial^2\boldsymbol{\phi}_a(x)}{\partial x^2}\right)^T dx \tag{13}$$

where EI_a is the bending stiffness of the appendage. Constructing the lagrangian:

$$\mathcal{L} = \mathcal{T} - \mathcal{V} \tag{14}$$

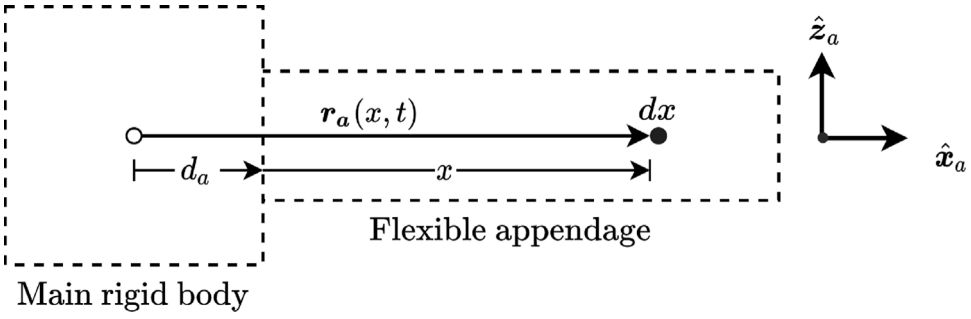

Fig. 2. Position of mass dx along each appendage.

the Euler–Lagrange equations can be considered in order to derive the ordinary differential equations:

$$\frac{d}{dt}\left(\frac{\partial \mathcal{L}}{\partial \boldsymbol{\omega}}\right) = 0 \tag{15}$$

$$\frac{d}{dt}\left(\frac{\partial \mathcal{L}}{\partial \dot{\boldsymbol{\eta}}_a(t)}\right) - \frac{\partial \mathcal{L}}{\partial \boldsymbol{\eta}_a(t)} = 0 \tag{16}$$

It is assumed that vibrations in the appendages have a negligible effect on the overall inertia of the satellite. This gives the body rate differential equation:

$$\mathbf{I}\dot{\boldsymbol{\omega}} + \mathbf{A}_w\boldsymbol{u} + \boldsymbol{\Gamma}_1^T\ddot{\boldsymbol{\eta}}_1 + \boldsymbol{\Gamma}_2^T\ddot{\boldsymbol{\eta}}_2 + [\boldsymbol{\omega}]_\times\left(\mathbf{I}\boldsymbol{\omega} + \mathbf{I}_w\boldsymbol{\omega}_w + \boldsymbol{\Gamma}_1^T\dot{\boldsymbol{\eta}}_1 + \boldsymbol{\Gamma}_2^T\dot{\boldsymbol{\eta}}_2\right) = 0 \tag{17}$$

where $\mathbf{I}$ is the total inertia of the satellite:

$$\mathbf{I} = \mathbf{I}_{hub} + \mathbf{I}_w + \rho_1\left(d_1^2L_1 + d_1L_1^2 + \frac{L_1^3}{3}\right)\left[\hat{\mathbf{x}}_1^B\right]_\times\left[\hat{\mathbf{x}}_1^B\right]_\times^T + \rho_2\left(d_2^2L_2 + d_2L_2^2 + \frac{L_2^3}{3}\right)\left[\hat{\mathbf{x}}_2^B\right]_\times\left[\hat{\mathbf{x}}_2^B\right]_\times^T \tag{18}$$

and $\boldsymbol{u}$, the control input, is simply the reaction wheel torque as seen in Eq. (2). Note that Eq. (18) is also used to give the total inertia for the rigid body model in Eq. (1). The matrices $\boldsymbol{\Gamma}_a$ give the coupling between the rigid body and each appendage which in the continuous case can be defined as:

$$\boldsymbol{\Gamma}_a^T = \rho_a\int_0^{L_a}(d_a + x)\left[\hat{\mathbf{x}}_a^B\right]_\times\hat{\mathbf{z}}_a^B\boldsymbol{\phi}_a^T(x)\,dx \tag{19}$$

Additionally the differential equation for each appendage can be defined as:

$$\mathbf{M}_a\ddot{\boldsymbol{\eta}}_a + \boldsymbol{\Gamma}_a\dot{\boldsymbol{\omega}} + \mathbf{K}_a\boldsymbol{\eta}_a = 0 \tag{20}$$

where the mass matrix $\mathbf{M}_a$ is given as:

$$\mathbf{M}_a = \rho_a\int_0^{L_a}\boldsymbol{\phi}_a(x)\boldsymbol{\phi}_a^T(x)\,dx \tag{21}$$

For the continuous case, an analytical solution to the modal shapes can be given [31]:

$$\phi_{a,m}(x) = \left(\cosh\frac{\gamma_{a,m}x}{L_a} - \cos\frac{\gamma_{a,m}x}{L_a}\right) - \frac{\cosh\gamma_{a,m} + \cos\gamma_{a,m}}{\sinh\gamma_{a,m} + sin\gamma_{a,m}} \times \left(\sinh\frac{\gamma_{a,m}x}{L_a} - \sin\frac{\gamma_{a,m}x}{L_a}\right) \tag{22}$$

where $\gamma_{a,m}$ is the solution to the equation:

$$\cos\gamma_{a,m}\cosh\gamma_{a,m} + 1 = 0 \tag{23}$$

which gives infinite solutions corresponding to the infinite number of natural frequencies, $\omega_n^{a,m}n$, for an infinite number of modes for each appendage:

$$\omega_n^{a,m} = \gamma_{a,m}^2\frac{EI_a}{\sqrt{\rho_aL_a^4}} \tag{24}$$

The equations of motion of the satellite with continuous flexible appendages are therefore defined. The derivation using the finite-element model will result in equations of the same form as seen in Eqs. (17) and (20), with the definitions of the mass ($\mathbf{M}_a$), stiffness ($\mathbf{K}_a$) and coupling matrices ($\boldsymbol{\Gamma}_a$) being altered. Additionally, the nondimensional displacements $\boldsymbol{\eta}_a$ and shapes $\boldsymbol{\phi}_a$ will correspond to the displacement and bending at each of the nodes of the finite-element model in this case.

An example of a two-element beam can be seen in Fig. 3 with three nodes attached to the ends of each finite element (seen in red in Fig. 3). Each node has two degrees of freedom, displacement and bending. The deflection of each element of the appendage can be given as:

$$w_{a,e}(x,t) = \boldsymbol{\phi}_{a,e}(x)^T\boldsymbol{\Lambda}_{a,e}\boldsymbol{\eta}_a(t) \tag{25}$$

where the matrix $\boldsymbol{\Lambda}_{a,e}$ selects the nodal displacements $\boldsymbol{\eta}_a$ that affect the element e. An example of a two-element appendage as seen in Fig. 3 can be seen:

$$\boldsymbol{\Lambda}_{i,1} = \begin{bmatrix}1&0&0&0&0&0\\0&1&0&0&0&0\\0&0&1&0&0&0\\0&0&0&1&0&0\end{bmatrix} \tag{26}$$

$$\boldsymbol{\Lambda}_{i,2} = \begin{bmatrix}0&0&1&0&0&0\\0&0&0&1&0&0\\0&0&0&0&1&0\\0&0&0&0&0&1\end{bmatrix} \tag{27}$$

The deflection across each element of the beam is assumed to be cubic giving the shape function $\boldsymbol{\phi}(x)_{a,e}$ for each element [31]:

$$\boldsymbol{\phi}(x)_{a,e} = \begin{bmatrix}1 - 3\left(\frac{x}{l_{a,e}}\right)^2 + 2\left(\frac{x}{l_{a,e}}\right)^3\\ x - 2l_{a,e}\left(\frac{x}{l_{a,e}}\right)^2 + l_{a,e}\left(\frac{x}{l_{a,e}}\right)^3\\ 3\left(\frac{x}{l_{a,e}}\right)^2 - 2\left(\frac{x}{l_{a,e}}\right)^3\\ -l_{a,e}\left(\frac{x}{l_{a,e}}\right)^2 + l_{a,e}\left(\frac{x}{l_{a,e}}\right)^3\end{bmatrix} \tag{28}$$

where $l_{a,e}$ is the length of each element:

$$l_{a,e} = \frac{L_a}{N_e} \tag{29}$$

where N_e is the number of elements in each appendage. Note that for the finite-element model, we will only ever need four shape functions. The deflection across the appendage will be a piecewise cubic interpolation between each node of the finite-element model. For the continuous model, the number of shape functions will correspond directly to the number of modes included, with each shape describing the deflection across the whole appendage. In the finite-element model, $\boldsymbol{\eta}_a$ corresponds to the displacement or bending at each of the nodes. Instead, in the continuous model, $\boldsymbol{\eta}_a$ corresponds to the contribution of each mode to the overall deflection in the appendage. The notation is used here interchangeably simply to maintain a consistent form as shown in Eqs. (17) and (20).

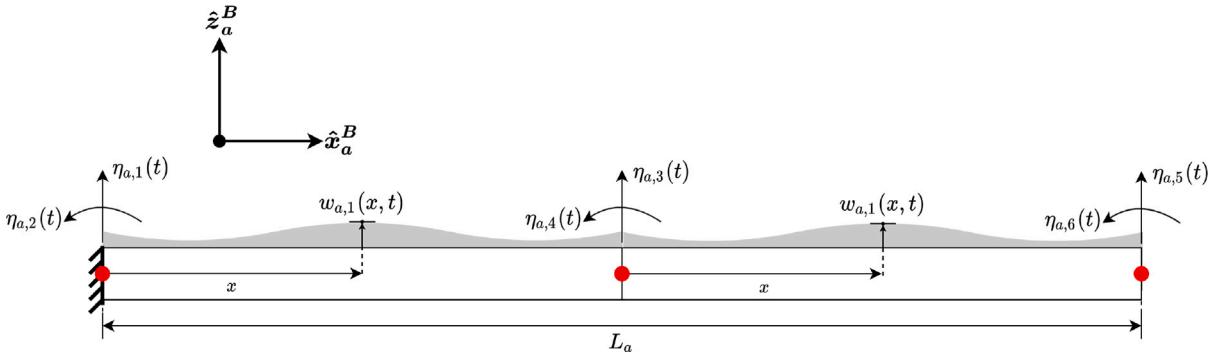

Fig. 3. Finite-element appendage: two-element example (nodes in red). (For interpretation of the references to colour in this figure legend, the reader is referred to the web version of this article.)

The spring stiffness of each element $\mathbf{K}_{a,e}$ is defined as:

$$\mathbf{K}_{a,e} = \frac{EI_a}{l_{a,e}^3}\begin{bmatrix} 12 & 6l_{a,e} & -12l_{a,e} & 6l_{a,e} \\ 6l_{a,e} & 4l_{a,e}^2 & -6l_{a,e} & 2l_{a,e}^2 \\ -12 & -6l_{a,e} & 12 & -6l_{a,e} \\ 6l_{a,e} & 2l_{a,e}^2 & -6l_{a,e} & l_{a,e}^2 \end{bmatrix} \tag{30}$$

with the element mass matrix $\mathbf{M}_{a,e}$ similarly:

$$\mathbf{M}_{a,e} = \frac{\rho_a l_{a,e}}{420}\begin{bmatrix} 156 & 22l_{a,e} & 54 & -13l_{a,e} \\ 22l_{a,e} & 4l_{a,e}^2 & 13l_{a,e} & -3l_{a,e}^2 \\ 54 & 13l_{a,e} & 156 & -22l_{a,e} \\ -13l_{a,e} & -3l_{a,e}^2 & -22l_{a,e} & 4l_{a,e}^2 \end{bmatrix} \tag{31}$$

Using the transformation matrices $\mathbf{\Lambda}_{a,e}$ we can get the overall stiffness and mass matrices:

$$\mathbf{K}_a = \sum_{e=1}^{N_e} \mathbf{\Lambda}_{a,e}^T \mathbf{K}_{a,e} \mathbf{\Lambda}_{a,e} \tag{32}$$

$$\mathbf{M}_a = \sum_{e=1}^{N_e} \mathbf{\Lambda}_{a,e}^T \mathbf{M}_{a,e} \mathbf{\Lambda}_{a,e} \tag{33}$$

The cantilever boundary conditions can then be applied by simply constraining the first node's displacement and bending, as seen in Fig. 3, by deleting the first two rows and columns of $\mathbf{K}_a$ and $\mathbf{M}_a$. The first two columns of $\mathbf{\Lambda}_{a,e}$ are also deleted.

Finally the coupling between the rigid and flexible dynamics for the finite-element model can be found by considering contributions from each finite element:

$$\mathbf{\Gamma}_a = \left(\rho_a \int_0^{l_{a,e}} \left[\sum_{e=1}^{N_e} \left(d_a + (e-1)l_{a,e} + x \right) \mathbf{\Lambda}_{a,e}^T \right] \boldsymbol{\phi}(x) dx \right) \left[\hat{\boldsymbol{x}}_a^B \right]_\times \hat{\boldsymbol{z}}_a^B \tag{34}$$

The natural frequencies of the finite-element model can be found by considering the solutions to the eigenvalue problem:

$$\lambda_{a,m} \boldsymbol{\eta}_{a,m} = -\mathbf{M}_a^{-1} \mathbf{K}_a \boldsymbol{\eta}_{a,m} \tag{35}$$

with the natural frequency being given as:

$$\omega_n^{a,m} = \| \sqrt{\lambda_{a,m}} \| \tag{36}$$

Taking the corresponding eigenvectors, $\boldsymbol{\eta}_{a,m}$, and substituting them into Eq. (25) the finite-element model's modal shapes can be found. As mentioned previously the satellite used as an example for this work includes two flexible appendages and four reaction wheels. The nominal parameters for this configuration can be seen in Table 1.

The normalised modal shapes for both the continuous appendage and a $N_e = 6$ finite-element appendage can be seen in Fig. 4 with their corresponding natural frequencies. It can therefore be seen that the modal response of the finite-element model has been verified against the analytical continuous model.

It has previously been mentioned that as the number of finite elements is increased, the number of flexible modes also increases. The higher-order modes will however have much less of an impact on the attitude dynamics of the satellite and therefore special attention is paid to the convergence of the first two modes of the finite-element model.

The convergence of the natural frequencies of the first and second modes can be seen in Fig. 5. It can be seen that after the 3rd or 4th finite element there is not much further relative improvement to the approximation of the first two mode frequencies. This will be worth considering when viewing the results of the model-based controller later in this paper.

Next the first two modal shapes for both the continuous and finite-element models are integrated across the appendage and compared in Fig. 6. The modal shapes will affect the coupling between the rigid and flexible modes and therefore may have an impact on attitude-tracking performance. It can be seen again that after the 3rd of 4th element is added the accuracy of the first two modal shapes does not change much. It can be seen however that the modal shapes do not converge as closely to the continuous model as the natural frequencies did. This is most likely due to the limitation of the assumed cubic shape of each element. It will be seen later in this paper if this has any detrimental effect on the model-based controller.

The attitude dynamics of a satellite with flexible appendages can be fully described through the ordinary differential equations given by Eqs. (4), (17) and (20). The "real" system that is used for testing the performance of the model-based controller uses a continuous analytical representation of each appendage's flexible dynamics using Eqs. (13), (19) and (21)–(23). The continuous model will be truncated after the 10th mode, $N_\phi = 10$, as this gave a good balance between computational effort and accuracy. This was confirmed by reproducing almost identical results when the number of modes was increased to 20. The finite-element appendage representation that will be utilised by the model-based controller is defined through Eqs. (28)–(34). Investigation into the effects of model fidelity, number of finite-elements, and model parameter uncertainty on the performance of the model-based controller will be carried out later in this paper.

3. Methodology

3.1. Integral inverse simulation algorithm

The integral inverse simulation method, first developed by Hess and Gao [18], and then explored further by Rutherford and Thomson [19], who coined it the generic inverse simulation (InvSim) method *GENISA*, is the method that is used in this work. A dynamic system can generally be defined as a system of nonlinear equations:

$$\dot{\boldsymbol{x}} = \boldsymbol{f}(\boldsymbol{x}, \boldsymbol{u}) \tag{37}$$

$$\boldsymbol{y} = \boldsymbol{g}(\boldsymbol{x}, \boldsymbol{u}) \tag{38}$$

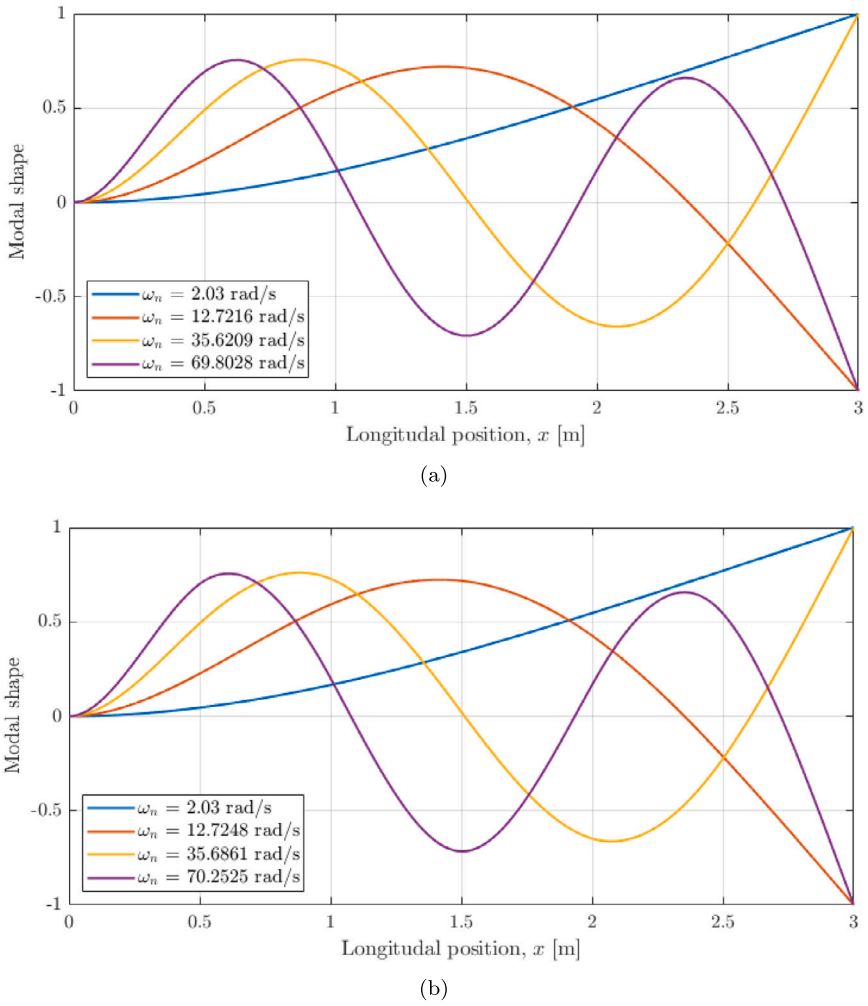

Fig. 4. First four normalised modal shapes of (a) continuous and (b) $N_e = 6$ finite-element model.

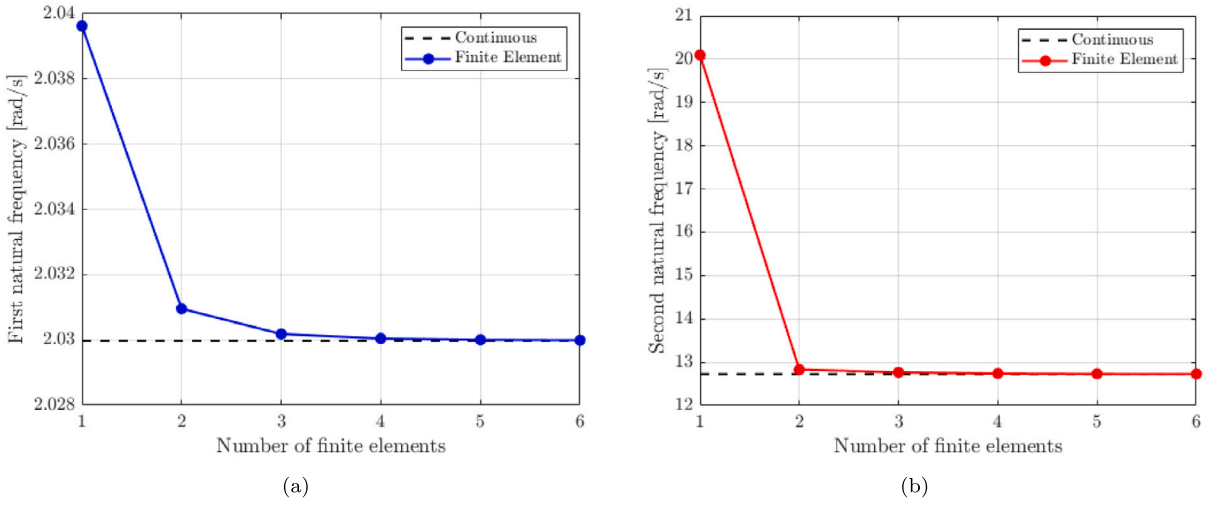

Fig. 5. Natural frequency convergence of (a) first mode, and (b) second mode.

where $\boldsymbol{f}(\cdot)$ contains a set of ordinary differential equations giving the state derivative $\dot{\boldsymbol{x}}$ in terms of the system state $\boldsymbol{x}$ and input $\boldsymbol{u}$. The function $\boldsymbol{g}(\cdot)$ gives the output states of the system $\boldsymbol{y}$. The inverse simulation process is therefore concerned with finding a solution for the input $\boldsymbol{u}(t)$, that gives a desired output $\boldsymbol{y}_d(t)$.

The desired output reference is first discretised by a user-defined control step T, giving a time series of desired output states, $\boldsymbol{y}_d[kT]$. The actual states and output states of the system can be given as:

$$\boldsymbol{x}[(k+1)T] = \int_{kT}^{(k+1)T} \dot{\boldsymbol{x}}[kT]\, dt + \boldsymbol{x}[kT] \tag{39}$$

Table 1
Nominal satellite model parameters.

Parameter	Value	Description
I_{hub}	$\begin{bmatrix} 500 & -10 & -20 \\ -10 & 400 & -30 \\ -20 & -30 & 350 \end{bmatrix}$ kg m^2	Inertia tensor of the main rigid hub at the centre of the satellite measured in body axes
$[L_1\ L_2]$	[3 3] m	Total length of each appendage
$[m_1\ m_2]$	[100 100] kg	Total mass of each appendage
$[d_1\ d_2]$	[1 1] m	Distance from the centre of the main hub to the root of each appendage
$[EI_1\ EI_2]$	[900 900] N m^2	Bending stiffness of each appendage
$[\hat{\boldsymbol{x}}_1^B\ \hat{\boldsymbol{x}}_2^B]$	$\begin{bmatrix} -1 & 1 \\ 0 & 0 \\ 0 & 0 \end{bmatrix}$	Unit vectors defining the longitudinal direction of each appendage
$[\hat{\boldsymbol{z}}_1^B\ \hat{\boldsymbol{z}}_2^B]$	$\begin{bmatrix} 0 & 0 \\ 0 & 0 \\ 1 & 1 \end{bmatrix}$	Unit vectors defining the transverse/flexing direction of each appendage
$\mathbf{A}_w$	$\begin{bmatrix} 1 & 0 & 0 & 1/\sqrt{3} \\ 0 & 1 & 0 & 1/\sqrt{3} \\ 0 & 0 & 1 & 1/\sqrt{3} \end{bmatrix}$	Reaction wheel actuator distribution matrix. Each column designates a reaction wheel's angular momentum vector within the body fixed axes
I_w	0.1 kg m^2	Inertia of each reaction wheel

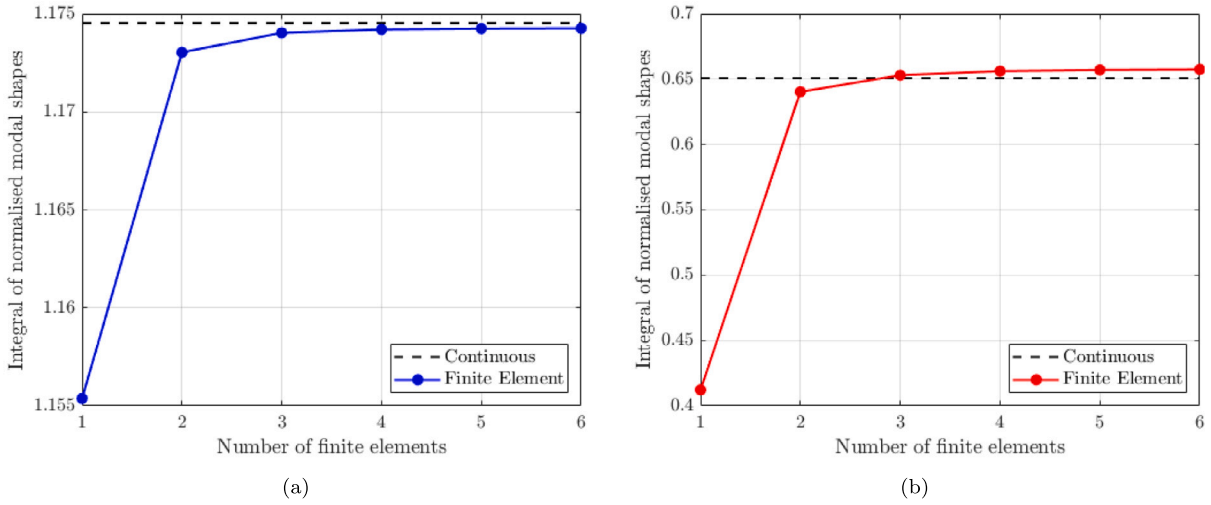

Fig. 6. Modal shape convergence of (a) first mode, and (b) second mode.

$$\boldsymbol{y}[(k+1)T] = \boldsymbol{g}\{\boldsymbol{x}[(k+1)T],\ \boldsymbol{u}[kT]\} \tag{40}$$

where the integration can be solved numerically using the Runge–Kutta method, with an integration step size Δt that should be sufficiently small to ensure numerical stability given the speed of the system dynamics. The error between the actual and desired output states, $\boldsymbol{\delta y}$, is therefore defined:

$$\boldsymbol{\delta y} = \boldsymbol{y}[(k+1)T] - \boldsymbol{y}_d[(k+1)T] = \boldsymbol{g}\{\boldsymbol{x}[(k+1)T],\ \boldsymbol{u}[kT]\} - \boldsymbol{y}_d[(k+1)T] \tag{41}$$

A suitable numerical method can then be employed to find a solution for $\boldsymbol{u}[kT]$ that satisfies $\boldsymbol{\delta y} = 0$. Several numerical methods have been employed such as Newton–Raphson (NR) [18,19], local optimisation [32] or search-based algorithms [32]. For this work, the NR method is sufficient. This involves the formation of a Jacobian of partial derivatives of each output state, y_i, with respect to each input, u_j:

$$\mathbf{J}_n = \begin{bmatrix} \frac{\partial y_1}{\partial u_1} & \frac{\partial y_1}{\partial u_2} & \cdots & \frac{\partial y_1}{\partial u_{N_u}} \\ \frac{\partial y_2}{\partial u_1} & \frac{\partial y_2}{\partial u_2} & \cdots & \frac{\partial y_2}{\partial u_{N_u}} \\ \vdots & \vdots & \ddots & \vdots \\ \frac{\partial y_{N_u}}{\partial u_1} & \frac{\partial y_{N_u}}{\partial u_2} & \cdots & \frac{\partial y_{N_u}}{\partial u_{N_u}} \end{bmatrix} \tag{42}$$

where each partial derivative can be calculated through numerical central differencing:

$$\left.\frac{\partial y_i}{\partial u_j}\right|_k = \frac{g_{ij}\{\boldsymbol{x}[kT],\ u_j + \Delta u_j\}|_{k+1} - g_{ij}\{\boldsymbol{x}[kT], u_j - \Delta u_j\}|_{k+1}}{2\Delta u_j}. \tag{43}$$

where g_{ij} is a mapping of the jth input to the ith output, and Δu_j is a perturbation applied to the jth input. The Jacobian can then be inverted and used to update the control estimate for the current timestep:

$$\boldsymbol{u}_n[kT] = \boldsymbol{u}_{n-1}[kT] + \mathbf{J}_n^{-1}\boldsymbol{\delta y} \tag{44}$$

where n is the current NR iteration. The inverse of the Jacobian can directly be found when the number of controls and outputs are identical, $N_u = N_u$, giving a square Jacobian. In the redundant case, $N_u > N_u$, or the underactuated case, $N_u < N_u$, a Moore–Penrose pseudoinverse is required to obtain an inverse of the nonsquare Jacobian. In the redundant case, there will be multiple solutions for $\boldsymbol{u}$ with the Moore–Penrose pseudoinverse converging upon the solution that minimises the norm of $\boldsymbol{u}$ [33]. However, in under-actuated cases, good performance cannot be guaranteed with the pseudo-inverse only able to obtain a least-squares-fit solution. In the case of a nonsquare Jacobian, the use of local optimisation methods may give additional customisation of

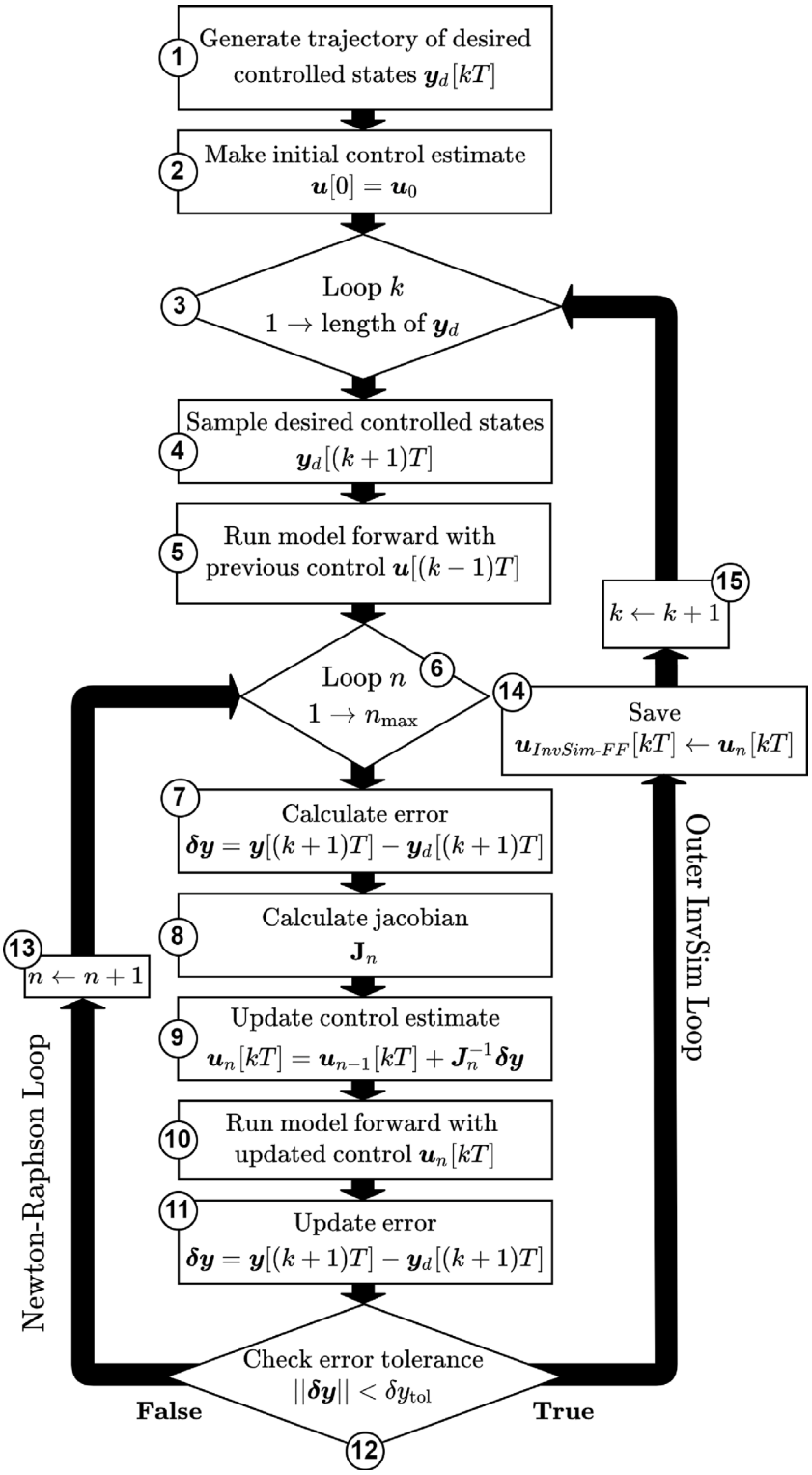

Fig. 7. The integral inverse simulation algorithm.

the control solution that is converged upon through the selection of appropriate cost functions [32]. For this work, however, the use of the Moore–Penrose pseudoinverse in the case of a nonsquare Jacobian is found to be acceptable.

The NR method iterates until a control solution is found that satisfies a user-defined tolerance δy_{tol}:

$$\|\boldsymbol{\delta y}\| < \delta y_{tol} \tag{45}$$

or a maximum number of NR iterations is reached, n_{max}. The full integral inverse simulation algorithm can be seen detailed in Fig. 7. The parameters for the InvSim that need to be chosen are the integration timestep Δt, control timestep T, initial control estimate for the first control timestep $\boldsymbol{u}_0$, a minimum control perturbation size to be applied during the numerical differencing Δu_{min}, NR tolerance δy_{tol}, and a maximum number of NR iterations n_{max}. Additionally, the differential order of the output states used can also be chosen, allowing for the

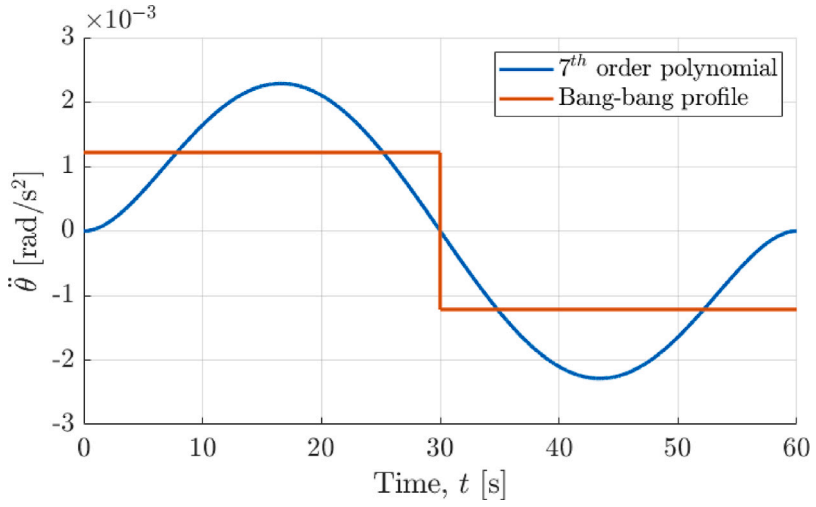

Fig. 8. Comparison of 7th order polynomial and bang–bang acceleration profiles for manoeuvre (a).

InvSim to target the position, velocity or acceleration of the reference trajectory. It has been found that the use of higher-order derivatives, such as velocity and acceleration, provides better numerical stability of the InvSim and avoids issues of chattering in some cases [19]. However, it was found in this work that the best accuracy in the InvSim solution was found when targeting the quaternion vector, $\boldsymbol{q}_{1:3}$, as the desired output states of the system, $\boldsymbol{y}_d$.

3.2. Path planning

Large-angle slew manoeuvres are used to test the hybrid and traditional PD tracking controllers. Spherical–linear-interpolation (SLERP) [34] and polynomials are used to produce smooth, low-jerk profiles to limit excitation of the flexible modes [3]. The smooth reference also ensures convergence of the InvSim algorithm employed in Section 3.1. Alternatively, a low-pass filter could be implemented to smooth a step reference before it is inverted by the InvSim [21]. A comparison of 7th order polynomial and bang–bang acceleration profiles, with the same manoeuvre duration, can be seen in Fig. 8. The polynomial profile minimises jerk at the expense of a higher maximum acceleration when compared to a bang–bang profile of the same duration.

The 7th order polynomial profile, $\theta(t)$, can be used to move along the shortest path between an initial quaternion, $\boldsymbol{q}_0$, and final quaternion, $\boldsymbol{q}_f$, using SLERP:

$$\boldsymbol{q}_d(t) = \frac{\sin((1-\theta(t))\delta_0)}{\sin(\delta_0)}\boldsymbol{q}_0 + \frac{\sin(\theta(t)\delta_0)}{\sin(\delta_0)}\boldsymbol{q}_f \tag{46}$$

where δ_0 is half the angle between the initial and final quaternions, given by:

$$\delta_0 = \cos^{-1}(\boldsymbol{q}_0 \cdot \boldsymbol{q}_f) \tag{47}$$

The PD tracking control law, detailed later in this paper, will make use of both the body rate and body acceleration profiles of the attitude tracking manoeuvre. These can be found by first calculating the first and second over derivatives of the quaternion SLERP paths:

$$\dot{\boldsymbol{q}}_d(t) = \frac{-\dot{\theta}(t)\delta_0\cos((1-\theta(t))\delta_0)}{\sin(\delta_0)}\boldsymbol{q}_0 + \frac{\dot{\theta}(t)\delta_0\cos(\theta(t)\delta_0)}{\sin(\delta_0)}\boldsymbol{q}_f \tag{48}$$

$$\begin{aligned}\ddot{\boldsymbol{q}}_d(t) = {} & \frac{-\ddot{\theta}(t)\delta_0\cos((1-\theta(t))\delta_0) - \dot{\theta}(t)^2\delta_0^2\sin((1-\theta(t))\delta_0)}{\sin(\delta_0)}\boldsymbol{q}_0 \\ & + \frac{\ddot{\theta}(t)\delta_0\cos(\theta(t)\delta_0) - \dot{\theta}(t)^2\delta_0^2\sin(\theta(t)\delta_0)}{\sin(\delta_0)}\boldsymbol{q}_f\end{aligned} \tag{49}$$

with the 7th order polynomial, $\theta(t)$, and its derivatives, $\dot{\theta}(t)$ and $\ddot{\theta}(t)$, defined as:

$$\theta(t) = a_4t^7 + a_3t^6 + a_2t^5 + a_1t^4 \tag{50}$$

$$\dot{\theta}(t) = 7a_4t^6 + 6a_3t^5 + 5a_2t^4 + 4a_1t^3 \tag{51}$$

$$\ddot{\theta}(t) = 42a_4t^5 + 30a_3t^4 + 20a_2t^3 + 12a_1t^2 \tag{52}$$

where the coefficients can be calculated based on a given duration, or time-to-move, of the manoeuvre, t_{move}:

$$\begin{aligned} a_4 &= \frac{-20}{t_{move}^7} \quad a_3 = \frac{70}{t_{move}^6} \\ a_2 &= \frac{-84}{t_{move}^5} \quad a_1 = \frac{35}{t_{move}^4} \end{aligned} \tag{53}$$

The inverse quaternion kinematics can then be used to obtain the desired body rate, $\boldsymbol{\omega}_d$, and body acceleration, $\dot{\boldsymbol{\omega}}_d$, of the SLERP path:

$$\boldsymbol{\omega}_d = 2\begin{bmatrix} -\boldsymbol{q}_{d,1:3}^T \\ q_{d,0}\,\mathbf{I}_{3\times3} + [\boldsymbol{q}_{\boldsymbol{d},\mathbf{1:3}}]_\times \end{bmatrix}^T \dot{\boldsymbol{q}}_d \tag{54}$$

$$\dot{\boldsymbol{\omega}}_d = 2\begin{bmatrix} -\dot{\boldsymbol{q}}_{d,1:3}^T \\ \dot{q}_{d,0}\,\mathbf{I}_{3\times3} + [\dot{\boldsymbol{q}}_{d,1:3}]_\times \end{bmatrix}^T \dot{\boldsymbol{q}}_d + 2\begin{bmatrix} -\boldsymbol{q}_{d,1:3}^T \\ q_{d,0}\,\mathbf{I}_{3\times3} + [\boldsymbol{q}_{\boldsymbol{d},\mathbf{1:3}}]_\times \end{bmatrix}^T \ddot{\boldsymbol{q}}_d \tag{55}$$

For the purposes of this paper the final quaternion is set to $\boldsymbol{q}_f = [1\ \ 0\ \ 0\ \ 0]^T$ for every manoeuvre, with a uniformly random initial quaternion $\boldsymbol{q}_0$ [35]. The time-to-move is $t_{move} = 60$ s for all manoeuvres. Additionally, the final attitude position is held constant, with velocity and acceleration being zero, for 10 additional seconds to ensure no deviation from the final attitude.

3.3. Attitude tracking control design

Two control strategies are detailed in this section: a PD tracking controller with reference body acceleration feedforward and nonlinear cross-coupling compensation, and a hybrid control approach combining a linear PD controller with InvSim feedforward elements. First, the PD tracking controller will be derived with the body rate and attitude quaternion shown to be asymptotically stable assuming that the satellite is rigid [36]. The stability of both control approaches will then depend upon avoiding the excitation of the flexible modes that can cause instability. This is achieved through the minimisation of a jerk, as seen in Section 3.2, and ensuring that the frequency response of the closed loop system is significantly slower than the flexible modes. Appropriate tuning of the PD gains and numerical simulations will be presented later to show the validity of this approach and its limitations.

First, a PD tracking control law, with structure as seen in Fig. 9, is considered [23]:

$$\boldsymbol{u}_{PD} = -\mathbf{A}_w^+ \left[-k_p \delta\boldsymbol{q}_{1:3} - \mathbf{K_D}\delta\boldsymbol{\omega} + \mathbf{I}\left(\dot{\boldsymbol{\omega}}_d - [\boldsymbol{\omega}]_\times \mathbf{I}\boldsymbol{\omega}_d\right) + [\boldsymbol{\omega}]_\times \left(\mathbf{I}\boldsymbol{\omega} + \mathbf{I}_w \boldsymbol{\omega}_w\right)\right] \tag{56}$$

where k_p is the scalar proportional gain, $\mathbf{K_D}$ is the derivative gain matrix, $\delta\boldsymbol{q}_{1:3}$ is the vector component of the error quaternion, and $\delta\boldsymbol{\omega}$ is the error in the body rate:

$$\delta\boldsymbol{\omega} = \boldsymbol{\omega} - \boldsymbol{\omega}_d \tag{57}$$

where the desired body rate, $\boldsymbol{\omega}_d$, and desired body acceleration, $\dot{\boldsymbol{\omega}}_d$, are given in Eqs. (54) and (55) respectively. Additionally, the body axis torques are mapped to each of the reaction wheels using $\mathbf{A}_w^+$, the minimum-norm inverse [23]:

$$\mathbf{A}_w^+ = \mathbf{A}_w^T (\mathbf{A}_w \mathbf{A}_w^T)^{-1} \tag{58}$$

Next the closed-loop, rigid body dynamics are found in terms of body rate errors. First, the derivative of the body rate error is taken:

$$\dot{\delta\boldsymbol{\omega}} = \dot{\boldsymbol{\omega}} - \dot{\boldsymbol{\omega}}_d - [\boldsymbol{\omega}]_\times \boldsymbol{\omega}_d \tag{59}$$

rearranging and substituted into Eq. (1) along with the proposed control law, Eq. (56), and cancelling out terms gives the closed loop error dynamics:

$$\dot{\delta\boldsymbol{\omega}} = \mathbf{I}^{-1}\left[-k_p \delta\boldsymbol{q}_{1:3} - \mathbf{K_D}\delta\boldsymbol{\omega}\right] \tag{60}$$

Next, a candidate Lyapunov function similar to that in [22] is chosen, but in terms of quaternion error and body rate error to ensure stability in the tracking scenario:

$$V = \frac{1}{4}\delta\boldsymbol{\omega}^T \mathbf{I}\delta\boldsymbol{\omega} + \frac{1}{2}k_p \delta\boldsymbol{q}_{1:3}^T \delta\boldsymbol{q}_{1:3} + \frac{1}{2}k_p (1-\delta q_0)^2 \geq 0 \tag{61}$$

where δq_0 is the scalar component of the quaternion error. Next, the time derivative of the Lyapunov function is taken:

$$\dot{V} = \frac{1}{2}\delta\boldsymbol{\omega}^T \mathbf{I}\dot{\delta\boldsymbol{\omega}} + k_p \delta\boldsymbol{q}_{1:3}^T \dot{\delta\boldsymbol{q}}_{1:3} - k_p(1-\delta q_0)\dot{\delta q}_0 \tag{62}$$

using Eq. (4) the kinematics of the error quaternion can be found [22]:

$$\dot{\delta\boldsymbol{q}}_{1:3} = \frac{1}{2}\delta q_0 \delta\boldsymbol{\omega} + \frac{1}{2}\left[\delta\boldsymbol{q}_{1:3}\right]_\times \left(\boldsymbol{\omega} + \boldsymbol{\omega}_d\right) \tag{63}$$

$$\dot{\delta q}_0 = -\frac{1}{2}\delta\boldsymbol{q}_{1:3}^T \delta\boldsymbol{\omega} \tag{64}$$

substituting Eqs. (60), (63) and (64) into Eq. (62) gives:

$$\dot{V} = \frac{1}{2}\delta\boldsymbol{\omega}^T\left(-k_p\delta\boldsymbol{q}_{1:3} - \mathbf{K_D}\delta\boldsymbol{\omega}\right) + \frac{1}{2}k_p \delta\boldsymbol{q}_{1:3}^T\left[\delta q_0 \delta\boldsymbol{\omega} + \left[\delta\boldsymbol{q}_{1:3}\right]_\times \left(\boldsymbol{\omega} + \boldsymbol{\omega}_d\right)\right] + \frac{1}{2}k_p(1-\delta q_0)\delta\boldsymbol{q}_{1:3}^T \tag{65}$$

collecting and cancelling terms and considering the cross/dot product $\boldsymbol{a}\cdot(\boldsymbol{a}\times\boldsymbol{b}) = \boldsymbol{a}^T[\boldsymbol{a}]_\times \boldsymbol{b} = 0$:

$$\dot{V} = -\frac{1}{2}\delta\boldsymbol{\omega}^T \mathbf{K_D}\delta\boldsymbol{\omega} < 0 \tag{66}$$

Therefore stability is proven provided that $\mathbf{K_D}$ is positive definite with the body rate error $\lim_{t\to\infty}\delta\boldsymbol{\omega} = 0$. Furthermore asymptotic stability can be proven through consideration of Eq. (60) where it can be seen that $\lim_{t\to\infty}\delta\boldsymbol{\omega} = 0$ only if $\lim_{t\to\infty}\delta\boldsymbol{q}_{1:3} = 0$ to reach the equilibrium $\dot{\delta\boldsymbol{\omega}} = 0$. Additionally $\lim_{t\to\infty}\delta q_0 = 1$ simply through the unit quaternion constraint.

Next, the roots of a linearised form of the closed loop, rigid dynamics are found. This will allow for the PD control gains, k_p and $\mathbf{K_D}$, to be chosen to give a closed-loop response that does not excessively excite the flexible modes of the satellite, and thus ensure stability. Taking the closed loop dynamics, Eq. (60), and linearising the quaternion error kinematics around $\delta\boldsymbol{q}_{1:3} = [1\ 0\ 0\ 0]^T$:

$$\dot{\delta\boldsymbol{q}}_{1:3} \approx \frac{1}{2}\delta\boldsymbol{\omega} \tag{67}$$

and then by considering each axis separately, and ignoring off-diagonal inertia terms, the closed-loop dynamics can be expressed as:

$$\begin{bmatrix}\dot{\delta q}_i \\ \dot{\delta\omega}_i\end{bmatrix} = \begin{bmatrix}0 & \frac{1}{2} \\ -\frac{k_p}{I_i} & -\frac{K_{D,i}}{I_i}\end{bmatrix}\begin{bmatrix}\delta q_i \\ \delta\omega_i\end{bmatrix} \tag{68}$$

Giving the closed loop roots $\bar{\lambda}_i$:

$$\bar{\lambda}_i = -\frac{1}{2I_i}\left(K_{D,i} \pm \sqrt{K_{D,i}^2 - 2I_i k_p}\right) \tag{69}$$

which can be used to find the natural frequency, $\bar{\omega}_n^i$, damping ratio, $\bar{\zeta}_i$, and damped frequency $\bar{\omega}_\zeta^i$:

$$\bar{\omega}_n^i = \|\bar{\lambda}_i\| \tag{70}$$

$$\bar{\zeta}_i = \cos(\angle\ \bar{\lambda}_i) \tag{71}$$

$$\bar{\omega}_\zeta^i = \bar{\omega}_n^i \sqrt{1-\bar{\zeta}_i^2} \tag{72}$$

where $\angle\ \bar{\lambda}_i$ is the argument. Therefore, the PD control gains can be chosen to satisfy a desired closed-loop response. The results of this gain tuning will be seen later in this paper (see Fig. 9).

The hybrid control combines the linear PD feedback control elements with a feedforward offline InvSim control solution, as can be seen in Fig. 10. The full control law is given as:

$$\boldsymbol{u}_{hybrid} = \boldsymbol{u}_{InvSim\text{-}FF} + \mathbf{A}_w^+\left[-k_p\delta\boldsymbol{q}_{1:3} - \mathbf{K_D}\delta\boldsymbol{\omega}\right] \tag{73}$$

The InvSim feedforward component should provide a nominal control effort to track the attitude slew manoeuvre, compensating for the nonlinear elements seen in the PD tracking control law, Eq. (56), and compensating for the flexible effects of the satellite appendages. The linear PD elements in Eq. (73) can provide some robustness to uncertainty in the model used by InvSim and also deal with external disturbances. Assuming that the InvSim is accurate and provides the nominal control effort, the hybrid control law in Eq. (73) will give the approximately closed loop error dynamics seen in Eq. (68). Therefore Eqs. (69)–(72) can be used to find suitable gains k_p and $\mathbf{K_D}$ for both the PD tracking control law, Eq. (56), and the hybrid control law, Eq. (73).

4. Results

4.1. Controller tuning

It has been shown that the PD tracking controller seen in Eq. (56) is capable of stabilising the system if it were assumed to be rigid. However, it is possible for the system to be de-stabilised should the flexible modes of the satellite be excited sufficiently. Therefore, to avoid the excitation of these de-stabilising flexible modes a low jerk polynomial SLERP profile is used, as shown in Section 3.2, and the PD control gains will be tuned to ensure that the closed-loop response does not overly excite the flexible modes.

This can be done by first considering the lowest frequency flexible mode which has a natural frequency of approximately 2.03 rad/s. The PD gains should therefore be tuned to give a closed-loop frequency response that is sufficiently lower than 2.03 rad/s to ensure that the flexible modes do not trigger any instability. The consequences of not ensuring sufficient margin to the flexible modes can be seen in Fig. 11 which shows instability when using the hybrid controller to track a polynomial SLERP, with PD gains tuned for a damped closed-loop frequency of ≈2 rad/s and damping ratio ≈0.7. In this example, the system is completely known with the InvSim control effort providing good tracking by itself, however with the addition of the fast PD control elements the flexible modes have been excited sufficiently to induce instability. This will equally be the case for the PD tracking controller, as the proportional and derivative terms are the same.

If the PD controller is instead tuned to have a slower response, with damped natural frequency ≈1 rad/s and damping ratio ≈0.7, then

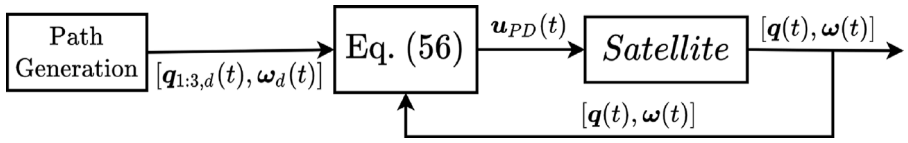

Fig. 9. PD tracking control structure.

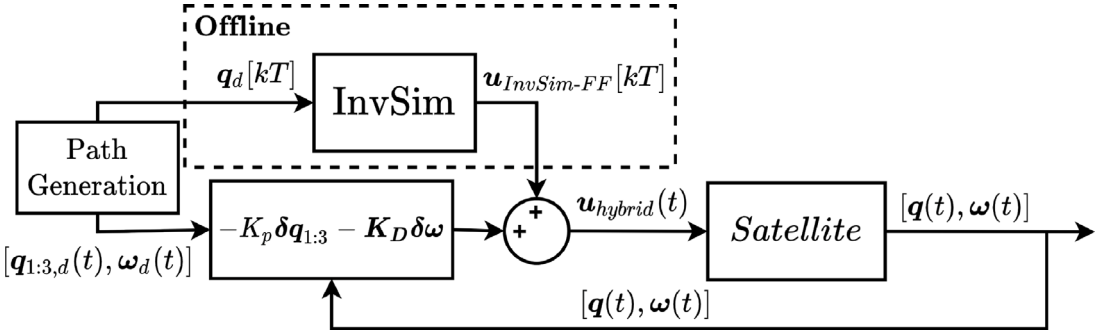

Fig. 10. Hybrid control: linear PD feedback with offline InvSim feedforward compensation.

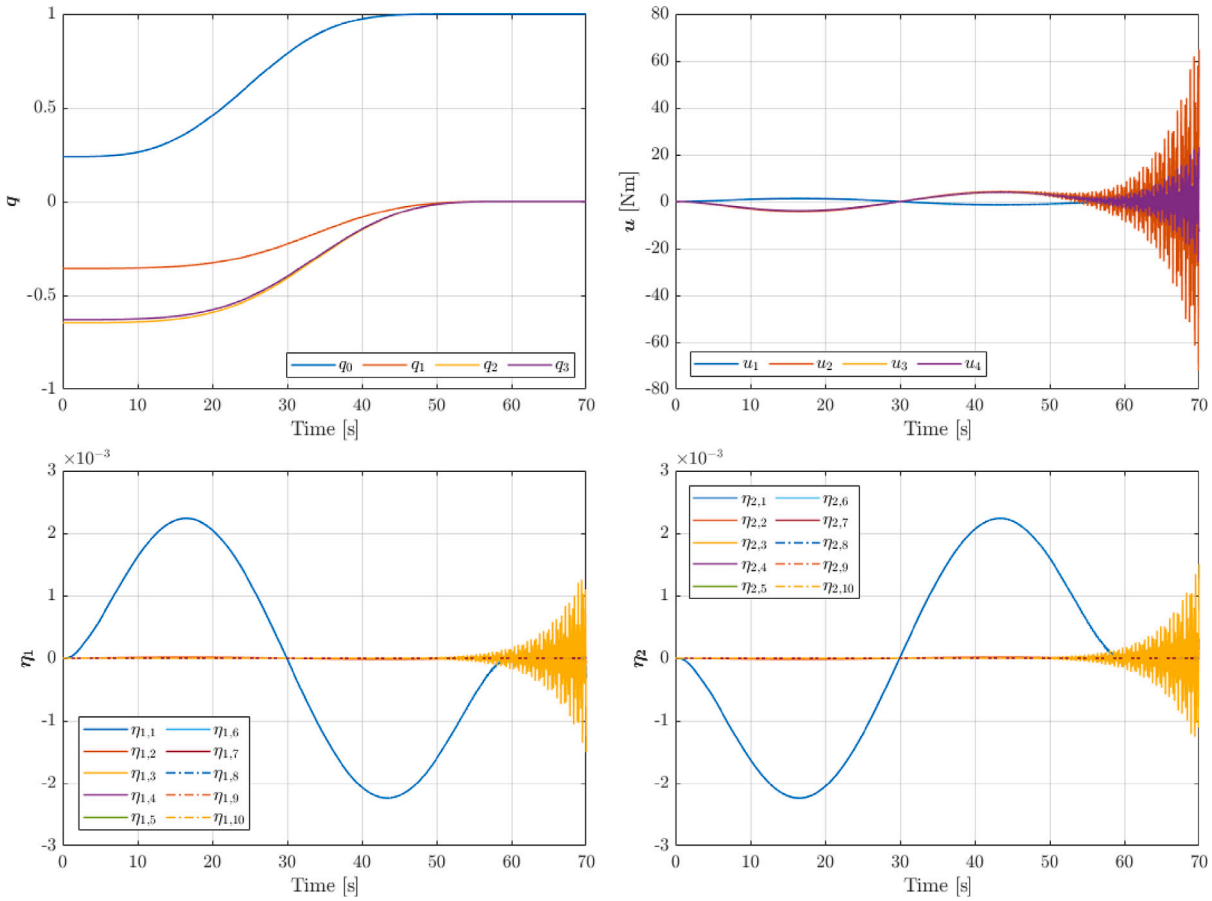

Fig. 11. Hybrid control unstable response: $\bar{\omega}_\zeta \approx 2$ rad/s, $\bar{\zeta} \approx 0.7$.

stability can be regained as seen in Fig. 12. The PD gains could be tuned to be even slower, providing a larger margin to the flexible modes, however as the attitude tracking performance of both the PD tracking controller and the hybrid controller need to be compared, tuning the PD gains to be too slow would give an unfair advantage to the hybrid approach. Therefore for a fair comparison, the PD gains for both controllers are given in Table 2 giving the response for the hybrid controller as seen in Fig. 12.

Table 2
PD control gains, $\bar{\omega}_\zeta \approx 1$ rad/s, $\bar{\zeta} \approx 0.7$.

k_p	3067
$\mathbf{K_D}$	diag(700,2500,2800)

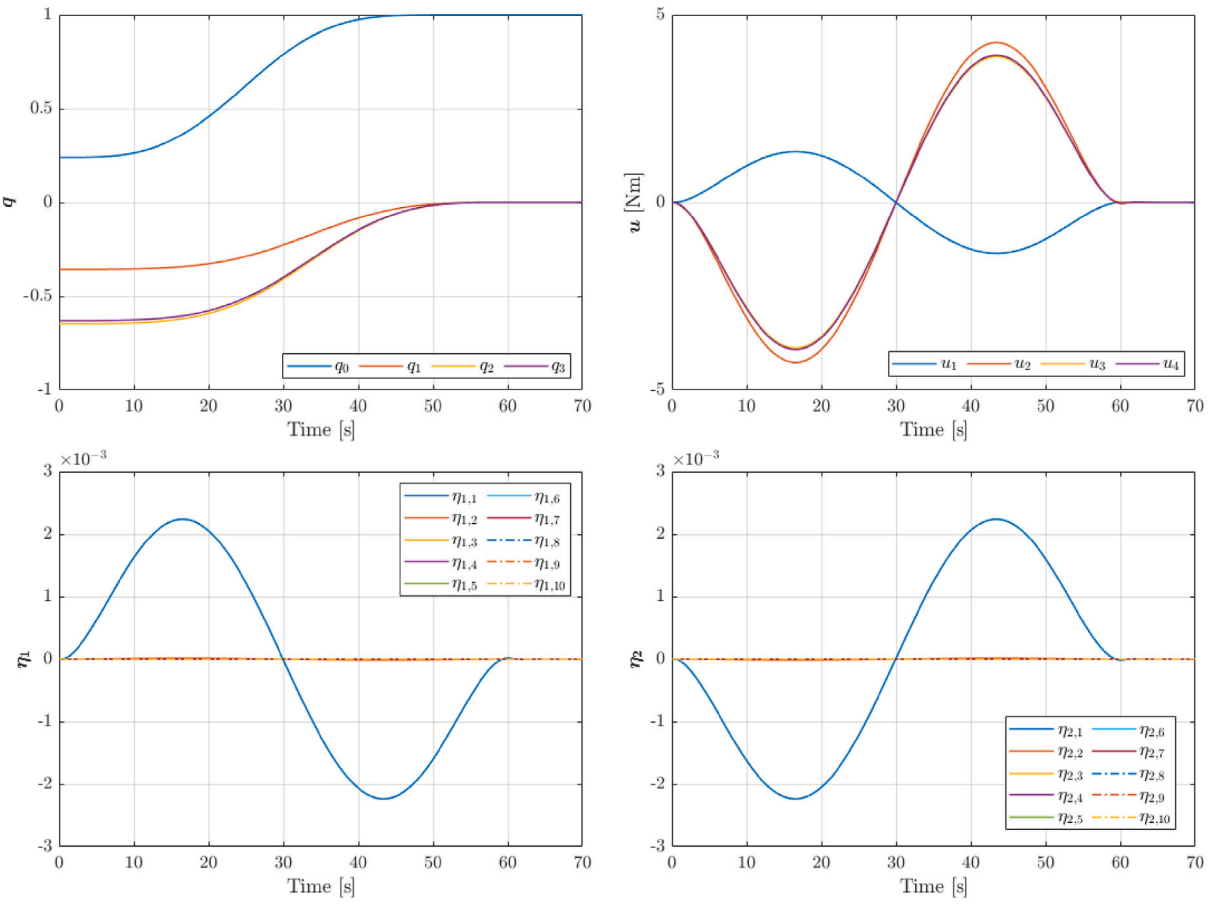

Fig. 12. Hybrid control stable response: $\bar{\omega}_\xi \approx 1$ rad/s, $\bar{\xi} \approx 0.7$.

The InvSim parameters used for the hybrid controller are shown in Table 3. It can be seen that, as the number of finite elements in the model increases, the integration timestep Δt needs to be decreased to ensure numerical stability. Fig. 13 shows the trend of the integration timestep required for different levels of model fidelity that can be utilised to produce the InvSim term in the hybrid controller. As the integration timestep decreases the computation time of the InvSim will increase considerably. For example, running InvSim using an $N_e = 6$ fidelity model will take ≈60× longer to run compared to an $N_e = 1$ fidelity model. As can be seen in Fig. 5(a), the first mode natural frequency does not converge much further after the 3rd or 4th finite element is added. The question, therefore, is posed: what level of model fidelity provides the best balance between the pointing performance of the model-based hybrid controller, and computational effort? It could be the case that the higher-fidelity models do not provide significant improvement in attitude-tracking performance, and therefore, using simpler, more computationally-efficient models may be preferable.

4.2. Monte-Carlo simulations

To test the validity and performance of the model-based hybrid controller and make comparisons with the PD tracking controller, a set of Monte-Carlo simulations was utilised. As mentioned previously, the continuous analytical modal solution is utilised as the "real" system with the InvSim used in the hybrid controller utilising different finite-element and rigid models to calculate the feedforward term. A set of 100 uniformly-random [35] quaternion SLERP polynomial manoeuvres are generated as shown in Section 3.2. Each controller will then be tested with the pointing error, $\delta\vartheta$, being used to quantify performance:

$$\delta\vartheta = 2\cos^{-1}(\boldsymbol{q}_d \cdot \boldsymbol{q}) \tag{74}$$

Table 3
Inverse simulation parameters.

Parameters		Values
Integration timestep, Δt (s)	Rigid	0.1
	$N_e = 1$	$0.03\dot{3}$
	$N_e = 2$	5×10^{-3}
	$N_e = 3$	2.08×10^{-3}
	$N_e = 4$	1.14×10^{-3}
	$N_e = 5$	7.23×10^{-4}
	$N_e = 6$	5.05×10^{-4}
Control timestep, T		0.1
Initial control estimate, $\boldsymbol{u}_0$		$[0\ 0\ 0\ 0]^T$ N m
Minimum control perturbation, Δu_{min}		1 N m
NR Error tolerance, ϵ_{tol}		1×10^{-16}
Maximum NR iterations, n_{max}		10

An additional set of Monte-Carlo simulations are run for the same 100 uniformly-random manoeuvres but in this case with the addition of uniform uncertainty in each of the model parameters. Each one of the 100 manoeuvres is run 100 times for each controller varying the uncertainty in the "real" model according to the ranges in Table 4. This is repeated for the hybrid controller for 7 different levels of model fidelity: a rigid model, and finite-element models ranging from $N_e = 1$ to $N_e = 6$. Therefore, 10,000 simulations are run for each hybrid controller and additionally for the PD tracking controller.

The results of these Monte-Carlo simulations, both with and without parameter uncertainty, can be seen in Fig. 14 in the form of boxplots. The centre of each box shows the median mean pointing error for a specific controller. The upper and lower bounds of the boxes show the 75th and 25th percentiles, meaning that the box itself contains

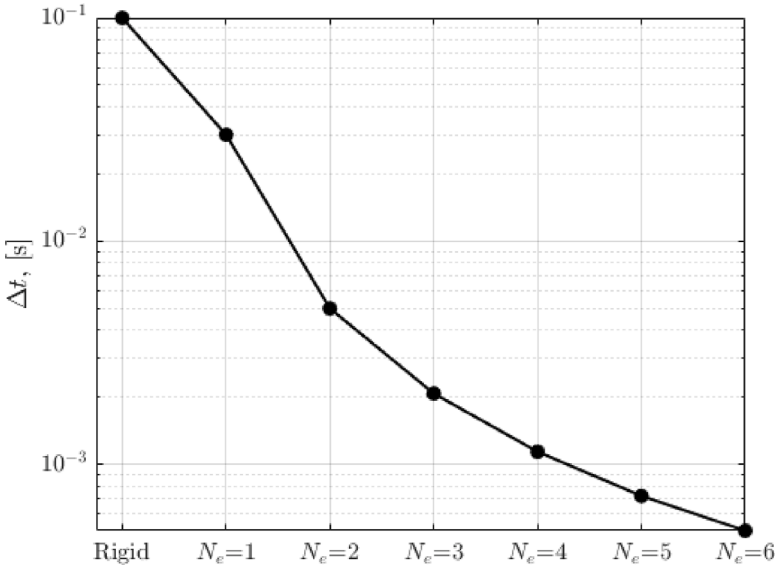

Fig. 13. Integration timestep for different model fidelities.

Table 4
Monte-Carlo parameter uncertainties.

Property	Uniform uncertainty
I_{hub}	±10
$[L_1\ L_2]$	±10% scale
$[m_1\ m_2]$	±10% scale
$[d_1\ d_2]$	±10% scale
$[EI_1\ EI_2]$	±10% scale
$[\hat{\mathbf{x}}_1^B\ \hat{\mathbf{x}}_2^B]$, $[\hat{\mathbf{z}}_1^B\ \hat{\mathbf{z}}_2^B]$	±5 deg misalignment
$\mathbf{A}_w$	±5 deg misalignment

50% of all of the results. The dotted whiskers show the absolute maximum and minimum mean pointing errors seen during the Monte-Carlo simulations for that specific controller.

It can be seen in the case where no parameter uncertainty is present that the hybrid controller performs better than the PD tracking controller for any level of model fidelity. The inclusion of the flexible modes in the InvSim further improves tracking performance giving an order of magnitude improvement over the PD tracking controller. However, it is interesting to note that there does not seem to be any noticeable pointing accuracy gained by increasing the number of finite elements included in the hybrid controller's model. Instead, it seems that, in the absence of parameter uncertainty, a one-element finite-element model is perfectly sufficient and increasing the number of elements will just add un-needed computational cost. This is most likely due to the fact that only the first few modes will have a significant impact on the rigid main hub, and therefore it may be that the one-element model provides sufficient accuracy in the first few modes to give good attitude tracking performance. This will be investigated in more detail in the next section.

Next, it can be seen that when uniform parameter uncertainties are applied during the Monte-Carlo simulations in the ranges set out in Table 4, the performance advantage of the hybrid controller is almost completely lost. Therefore, it can be concluded that accurate knowledge of the system parameters is needed to achieve significant performance advantages when using the hybrid control approach. The next section will look to further investigate this further to get a better understanding of how accurately the system parameters need to be known.

4.3. Sensitivity analysis

This section will further investigate the effects of model parameter uncertainty on controller performance, determine which uncertainties degrade performance the most, and ascertain the limits of the hybrid control approach. To this aim, a sensitivity analysis was performed on a hybrid controller that utilises 2 finite elements, a hybrid controller that utilises a rigid body model, and the PD tracking controller. This will allow the effects of using the InvSim feedforward term and the effect of the model fidelity used to be assessed independently.

First, the sensitivity of each controller to scalar uncertainty in the inertia tensor can be seen in Fig. 15, with an expanded close-up view on the right to highlight the difference between the hybrid controllers with the rigid and finite-element models. It can be seen that as the inertia uncertainty increases that both hybrid controllers approach the performance of the PD tracking controller. Looking more closely, the performance of the finite-element hybrid controller approaches that of the one utilising only a rigid body model very quickly. Most of the performance advantage gained by including the flexible modes in the hybrid controller is lost within the first 1%. It can therefore be deduced that with an uncertain inertia tensor only, hybrid control will perform better than PD alone unless the inertia uncertainty is very large. Additionally, including a finite-element model with the hybrid controller will give improved performance over using only a rigid body model if the inertia is well known, with uncertainty of <1%.

Next, assuming that the inertia of the satellite is known, the effects of uncertainty in the flexible modes can be seen in Fig. 16. First, it can be seen that as the coupling of the first flexible mode decreases, the performance of the finite-element hybrid controller approaches that of the rigid hybrid controller. As the effect of the flexible modes on the dynamics of the rigid hub is diminished, consideration of them in the controller design becomes inconsequential. Additionally, as the coupling increases, both hybrid controllers start to degrade in performance as there are additional torques on the main body due to flexing that is not being accounted for. Secondly, it can be seen that, as the uncertainty in the first natural frequency increases, the performance of the finite-element hybrid controller approaches that of the rigid hybrid controller. As the flexible modes become uncertain, their inclusion in the hybrid controller becomes inconsequential and performs similarly to a hybrid controller that does not consider the flexible modes at all. It can be seen that in the case of uncertainty in the flexible modes only, both hybrid controllers maintain a significant performance advantage over the PD tracking controller. It can also be seen that, to ensure the best performance of the finite-element hybrid controller, the uncertainty in the first mode's natural frequency needs to be maintained <0.5 rad/s. Looking at Fig. 5(a) it can be seen that the one-element finite-element model is well within this range, which explains why

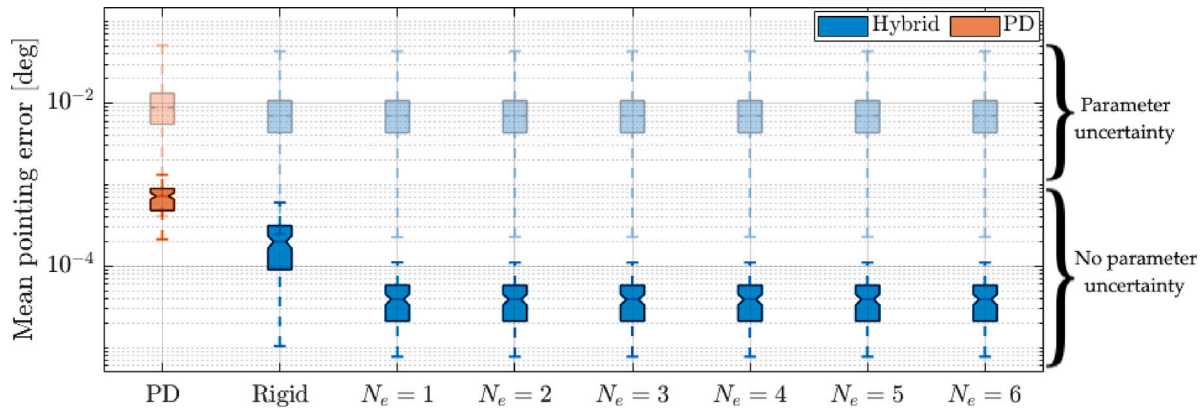

Fig. 14. Mean pointing error Monte-Carlo results: with parameter uncertainty (top), and without parameter uncertainty (bottom).

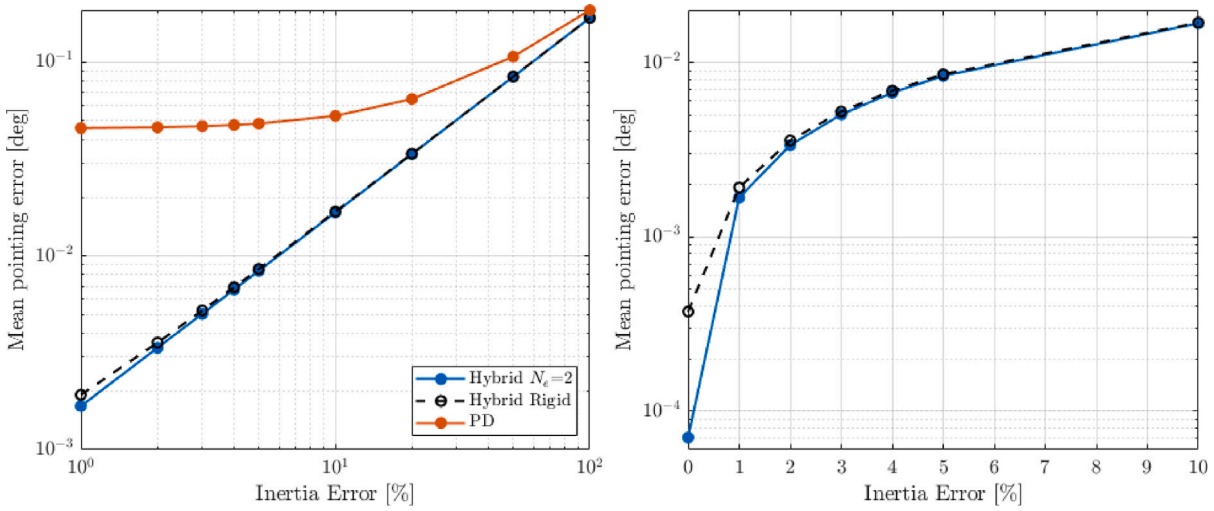

Fig. 15. Sensitivity to scalar inertia uncertainty, with zoomed-in view (right).

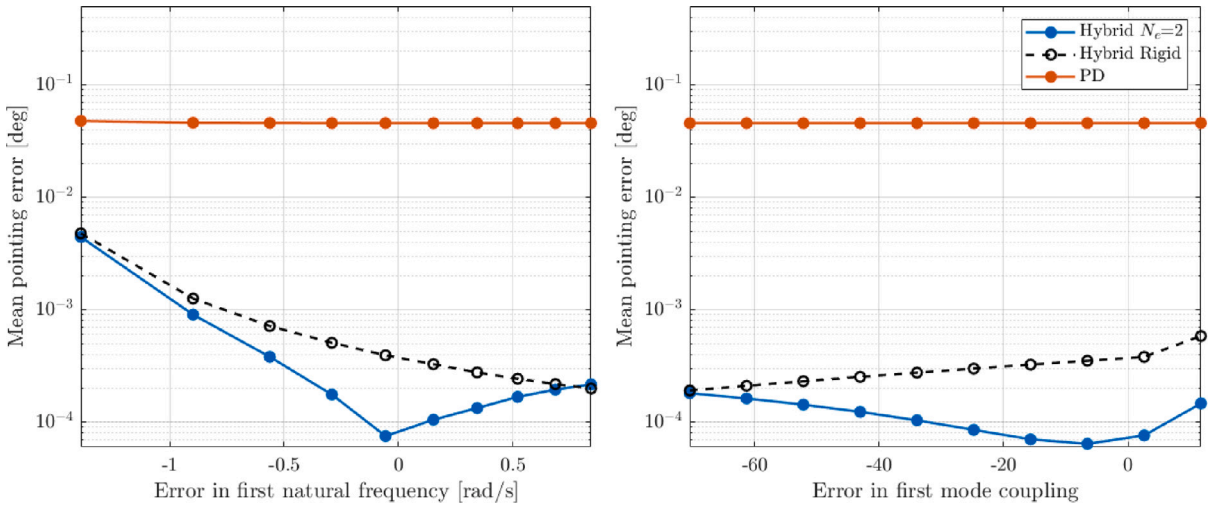

Fig. 16. Sensitivity to errors in flexible dynamics.

not much improvement was gained when increasing the number of finite-elements, Fig. 14.

An important note is that the ranges of uncertainties shown in Figs. 15 and 16 are limited by the stability of the controllers. Considering the inertia, Fig. 15, it can be seen that only positive inertia uncertainty was considered, i.e. when the inertia is greater than that assumed by the controllers. This is because, as the inertia decreases, the frequency response of the closed-loop dynamics increases (assuming the same PD control gains) according to Eqs. (69)–(72). The closed-loop frequency response will approach the natural frequencies of the flexible modes eventually triggering instability, as seen in Fig. 11. It can therefore be seen that the PD gains may need to be re-tuned to give

a slower response to ensure stability for a larger range of uncertainties in the inertia.

5. Conclusions

This work investigated the effects of model fidelity and parametric uncertainty on the performance of a proportional-derivative (PD) feedback controller with additional model inversion-based feedforward (hybrid control) for attitude tracking of a satellite with flexible appendages. Inverse simulation (InvSim) was used to produce the model inversion required, and comparisons of pointing accuracy performance were made with a traditional PD tracking control law. The stability of both controllers is dependent on the use of a low-jerk polynomial spherical–linear-interpolation (SLERP) path planning, and closed-loop pole placement to ensure sufficient margin to the flexible modes to ensure that excessive excitation is avoided. This approach attempts to avoid the requirement for direct measurement of the appendage flexing through the use of piezoelectric sensors, or for estimation of the flexible modal states.

The hybrid controller utilised models of varying fidelity, ranging from a rigid body assumption to models representing the flexible appendages with finite-element beams with a varying number of finite elements. The performance of the hybrid and PD tracking controllers was quantified by testing them on a model with continuous-beam appendages acting as the "real" system. The effects of using the different model fidelities in the hybrid controller, and of model parameter uncertainty, were investigated through the use of Monte-Carlo simulations and sensitivity analysis.

It was found that the use of the InvSim feedforward term in the hybrid controller improved pointing accuracy performance even when only the rigid body model was used. Performance was further improved with the inclusion of the flexible modes in the hybrid controller; however, no significant performance improvement was found when increasing the number of finite elements used. Therefore, when considering the additional computational cost of adding additional finite elements, it can be concluded that a one or two-element model is sufficient.

Next, it was found that, when considerable uncertainty is present in the model parameters, the performance gains of the hybrid controller are lost, with pointing accuracies being similar to the PD tracking controller. Upon further investigation, it was found that to maintain good attitude tracking of the hybrid controller, the uncertainty in the inertia should be <1%, and uncertainty in the first modal frequency <0.5 rad/s. In future, the addition of online parameter estimation would allow for accurate inertia and modal parameters to be found, which should allow convergence upon the ideal performance seen at the bottom of Fig. 14.

It was important to note that the inverse-model feedforward term could be obtained by other, more traditional means, such as Nonlinear Dynamic Inversion (NDI). However, InvSim provides this inverse-model feedforward term independently of the model used and does not require any re-derivation, should the model need to be changed at a later date. This is primarily due to the generic nature of the integral InvSim algorithm used, which treats the dynamic model as a black box, requiring no specific knowledge of the governing equations. This also suits InvSim as a *preliminary* control design tool, allowing for a control solution to readily be available as modifications are made to the design and allowing for detailed feasibility studies to be completed without the need to design a bespoke controller. The primary limitation of the InvSim approach was the higher computational overhead, which can be dealt with by calculating the feedforward term *a priori* given a planned reference trajectory, and the requirement for a model, which would already be required for NDI.

In future work, the addition of a state estimator may allow for the reconstruction of the flexible modal states, allowing for the InvSim to be updated with the full state of the system in real time. If the speed of the InvSim can be assured to be faster than real-time with an appropriate control frequency, then the InvSim could be used as a full-state feedback controller which should further improve attitude tracking performance over even the hybrid controller seen here. Additionally, an important note is that the flexible models used in this paper make the assumption that the deflections along the appendage will be small. Therefore, future investigations into the application of the same hybrid control approach with models that do not suffer this limitation may be of interest.

Declaration of competing interest

The authors declare that they have no known competing financial interests or personal relationships that could have appeared to influence the work reported in this paper.

Acknowledgements

This work is supported by the Engineering and Physical Sciences Research Council, United Kingdom, grant number 2442761.

References

[1] J.J. Kim, B. Agrawal, Experiments on Jerk-Limited Slew Maneuvers of a Flexible Spacecraft, in: Guidance, Navigation, and Control Conference and Exhibit, AIAA, 2006, http://dx.doi.org/10.2514/6.2006-6187.

[2] G. Fracchia, J.D. Biggs, M. Ceriotti, Analytical low-jerk reorientation maneuvers for multi-body spacecraft structures, Acta Astronaut. 178 (2021) 1–14, http://dx.doi.org/10.1016/j.actaastro.2020.08.020.

[3] M. Marshall, S. Pellegrino, Slew Maneuver Constraints for Agile Flexible Spacecraft, in: AIAA SCITECH 2023 Forum, 2023, http://dx.doi.org/10.2514/6.2023-1883.

[4] D. Gorinevsky, G. Vukovich, Nonlinear Input Shaping Control of Flexible Spacecraft Reorientation Maneuver, J. Guid. Control Dyn. 21 (2) (1998) 264–270, http://dx.doi.org/10.2514/2.4252.

[5] A. Tzes, S. Yurkovich, An adaptive input shaping control scheme for vibration suppression in slewing flexible structures, IEEE Trans. Control Syst. Technol. 1 (2) (1993) 114–121, http://dx.doi.org/10.1109/87.238404.

[6] H. Bang, C.-K. Ha, J. Hyoung Kim, Flexible spacecraft attitude maneuver by application of sliding mode control, Acta Astronaut. (ISSN: 0094-5765) 57 (11) (2005) 841–850, http://dx.doi.org/10.1016/j.actaastro.2005.04.009, URL https://www.sciencedirect.com/science/article/pii/S0094576505001700.

[7] Q. Hu, Robust adaptive sliding mode attitude maneuvering and vibration damping of three-axis-stabilized flexible spacecraft with actuator saturation limits, Nonlinear Dynam. (ISSN: 1573-269X) 55 (4) (2009) 301–321, http://dx.doi.org/10.1007/s11071-008-9363-1.

[8] Y. Miao, I. Hwang, M. Liu, F. Wang, Adaptive fast nonsingular terminal sliding mode control for attitude tracking of flexible spacecraft with rotating appendage, Aerosp. Sci. Technol. (ISSN: 1270-9638) 93 (2019) 105312, http://dx.doi.org/10.1016/j.ast.2019.105312, URL https://www.sciencedirect.com/science/article/pii/S127096381930567X.

[9] M. TayyebTaher, S.M. Esmaeilzadeh, Model predictive control of attitude maneuver of a geostationary flexible satellite based on genetic algorithm, Adv. Space Res. (ISSN: 0273-1177) 60 (1) (2017) 57–64, http://dx.doi.org/10.1016/j.asr.2017.03.013, URL https://www.sciencedirect.com/science/article/pii/S0273117717301862.

[10] A. Murilo, P.J. de Deus Peixoto, L.C. Gadelha de Souza, R.V. Lopes, Real-time implementation of a parameterized Model Predictive Control for Attitude Control Systems of rigid-flexible satellite, Mech. Syst. Signal Process. (ISSN: 0888-3270) 149 (2021) 107129, http://dx.doi.org/10.1016/j.ymssp.2020.107129.

[11] P. Iannelli, F. Angeletti, P. Gasbarri, A model predictive control for attitude stabilization and spin control of a spacecraft with a flexible rotating payload, Acta Astronaut. (ISSN: 0094-5765) (2022) http://dx.doi.org/10.1016/j.actaastro.2022.07.024, URL https://www.sciencedirect.com/science/article/pii/S0094576522003617.

[12] J. Wen, K. Kreutz-Delgado, The attitude control problem, IEEE Trans. Automat. Control (ISSN: 1558-2523) 36 (10) (1991) 1148–1162, http://dx.doi.org/10.1109/9.90228, VO - 36.

[13] G.C. Goodwin, S.F. Graebe, M.E. Salgado, et al., Control system design, Pearson, ISBN: 978-0139586538, 2000.

[14] J. Wan, J. Yu, High Precision Satellite Attitude Control Based on Feedforward Compensation, in: 6th World Congress on Intelligent Control and Automation, vol. 2, 2006, pp. 6261–6264, http://dx.doi.org/10.1109/WCICA.2006.1714287.

[15] E. Weerdt, E.-J. Kampen, D. Gemert, Q.P. Chu, J.A. Mulder, Adaptive Nonlinear Dynamic Inversion for Spacecraft Attitude Control with Fuel Sloshing, in: Guidance, Navigation and Control Conference and Exhibit, AIAA, 2008, http://dx.doi.org/10.2514/6.2008-7162.

[16] S. Tafazoli, On Attitude Recovery of Spacecraft using Nonlinear Control (Ph.D. thesis), 2005.

[17] D.J. Murray-Smith, A Review of Inverse Simulation Methods and Their Application, Int. J. Modell. Simul. (ISSN: 0228-6203) 34 (3) (2014) 120–125, http://dx.doi.org/10.2316/Journal.205.2014.3.205-5906, URL https://www.tandfonline.com/doi/abs/10.2316/Journal.205.2014.3.205-5906.

[18] R.A. Hess, C. Gao, Generalized algorithm for inverse simulation applied to helicopter maneuvering flight, J. Am. Helicopter Soc. 38 (4) (1993) 3–15, http://dx.doi.org/10.4050/jahs.38.4.3.

[19] S. Rutherford, D.G. Thomson, Improved methodology for inverse simulation, 2016/07/04, Aeronaut. J. (1968) 100 (993) (1996) 79–86, http://dx.doi.org/10.1017/S0001924000067348.

[20] M.L. Irel, T. Flessa, D. Thomson, E. McGookin, Comparison of nonlinear dynamic inversion and inverse simulation, J. Guid. Control Dyn. 40 (12) (2017) 3304–3309.

[21] L. Lu, D.J. Murray-Smith, E.W. McGookin, Investigation of inverse simulation for design of feedforward controllers, Math. Comput. Model. Dyn. Syst. 13 (5) (2007) 437–454, http://dx.doi.org/10.1080/13873950701344023.

[22] F.L. Markley, J.L. Crassidis, Fundamentals of Spacecraft Attitude Determination and Control, Springer New York, New York, NY, ISBN: 9781493908028, 2014, pp. 1–486, URL http://link.springer.com/10.1007/978-1-4939-0802-8.

[23] H. Schaub, J.L. Junkins, Nonlinear Spacecraft Stability and Control, Analytical Mechanics of Space Systems, ISBN: 978-1-62410-521-0, 2018, pp. 387–518.

[24] R. Gordon, K. Worrall, M. Ceriotti, Attitude Control of Satellites with Flexible Appendages Using Inverse Simulation, in: 73rd International Astronautical Congress (IAC), 2022.

[25] S. Devasia, Should model-based inverse inputs be used as feedforward under plant uncertainty? IEEE Trans. Automat. Control 47 (11) (2002) 1865–1871, http://dx.doi.org/10.1109/TAC.2002.804478.

[26] V.J. Modi, Attitude Dynamics of Satellites with Flexible Appendages- A Brief Review, J. Spacecr. Rockets 11 (11) (1974) 743–751, http://dx.doi.org/10.2514/3.62172.

[27] Q. Li, X. Ma, T. Wang, Reduced model for flexible solar sail dynamics, J. Spacecr. Rockets 48 (3) (2011) 446–453.

[28] S. Zhang, Y. Zhou, S. Cai, Fractional-Order PD Attitude Control for a Type of Spacecraft with Flexible Appendages, Fractal Fract. 6 (10) (2022) http://dx.doi.org/10.3390/fractalfract6100601,

[29] P.W. Likins, Finite element appendage equations for hybrid coordinate dynamic analysis, Int. J. Solids Struct. (ISSN: 0020-7683) 8 (5) (1972) 709–731, http://dx.doi.org/10.1016/0020-7683(72)90038-8, URL https://www.sciencedirect.com/science/article/pii/0020768372900388.

[30] M. Choi, C.J. Damaren, Structural Dynamics and Attitude Control of a Solar Sail Using Tip Vanes, J. Spacecr. Rockets (ISSN: 0022-4650) 52 (6) (2015) 1665–1679, http://dx.doi.org/10.2514/1.A33179.

[31] S.S. Rao, Vibration of continuous systems, 2nd Ed., John Wiley & Sons, Ltd, ISBN: 9781119424147, 2019.

[32] G. de Matteis, L.M. de Socio, A. Leonessa, Solution of aircraft inverse problems by local optimization, J. Guid. Control Dyn. 18 (3) (1995) 567–571, http://dx.doi.org/10.2514/3.21424.

[33] L. Lu, D.J. Murray-Smith, D.G. Thomson, Issues of numerical accuracy and stability in inverse simulation, Simul. Model. Pract. Theory 16 (9) (2008) 1350–1364, http://dx.doi.org/10.1016/j.simpat.2008.07.003.

[34] K. Shoemake, Animating Rotation with Quaternion Curves, in: Proceedings of the 12th Annual Conference on Computer Graphics and Interactive Techniques, Association for Computing Machinery, New York, NY, USA, 1985, pp. 245–254, http://dx.doi.org/10.1145/325334.325242.

[35] K. Shoemake, Uniform Random Rotations, in: D. KIRK (Ed.), Graphics Gems III (IBM Version), Morgan Kaufmann, San Francisco, ISBN: 978-0-12-409673-8, 1992, pp. 124–132, http://dx.doi.org/10.1016/B978-0-08-050755-2.50036-1, URL https://www.sciencedirect.com/science/article/pii/B9780080507552500361.

[36] D.P. Madonna, M. Pontani, P. Gasbarri, Nonlinear attitude maneuvering of a flexible spacecraft for space debris tracking and collision avoidance, Acta Astronaut. (ISSN: 0094-5765) (2023) http://dx.doi.org/10.1016/j.actaastro.2023.03.043.